

RESEARCH

Open Access



Retinal ganglion cell vulnerability to pathogenic tau in Alzheimer's disease

Miyah R. Davis¹, Edward Robinson¹, Yosef Koronyo¹, Elena Salobrar-Garcia^{2,3,4}, Altan Rentsendorj¹, Bhakta P. Gaire¹, Nazanin Mirzaei¹, Rakez Kaye^{5,6}, Alfredo A. Sadun^{7,8}, Alexander V. Ljubimov^{1,9,10}, Lon S. Schneider¹¹, Debra Hawes¹¹, Keith L. Black¹, Dieu-Trang Fuchs¹ and Maya Koronyo-Hamaoui^{1,10,12*}

Abstract

Pathological tau isoforms, including hyperphosphorylated tau at serine 396 (pS396-tau) and tau oligomers (Oligo-tau), are elevated in the retinas of patients with mild cognitive impairment (MCI) due to Alzheimer's disease (AD) and AD dementia. These patients exhibit significant retinal ganglion cell (RGC) loss, however the presence of tau isoforms in RGCs and their impact on RGC integrity, particularly in early AD, have not been studied. Here, we analyzed retinal superior temporal cross-sections from 25 MCI or AD patients and 16 age- and sex-matched cognitively normal controls. Using the RGC marker ribonucleic acid binding protein with multiple splicing (RBPMS) and Nissl staining, we found a 46–56% reduction in RBPMS⁺ RGCs and Nissl⁺ neurons in the ganglion cell layer (GCL) of MCI and AD retinas ($P < 0.05$ – 0.001). RGC loss was accompanied by soma hypertrophy (10–50% enlargement, $P < 0.05$ – 0.0001), nuclear displacement, apoptosis (30–50% increase, $P < 0.05$ – 0.01), and prominent expression of granulovacuolar degeneration (GVD) bodies and GVD-necroptotic markers. Both pS396-tau and Oligo-tau were identified in RGCs, including in hypertrophic cells. PS396-tau⁺ and Oligo-tau⁺ RGC counts were significantly increased by 2.1–3.5-fold in MCI and AD retinas versus control retinas ($P < 0.05$ – 0.0001). Tauopathy-laden RGCs strongly inter-correlated ($r_p = 0.85$, $P < 0.0001$) and retinal tauopathy associated with RGC reduction ($r_p = -0.40$ – (-0.64) , $P < 0.05$ – 0.01). Their abundance correlated with brain pathology and cognitive deficits, with higher tauopathy-laden RGCs in patients with Braak stages (V–VI), clinical dementia ratings (CDR=3), and mini-mental state examination (MMSE ≤ 26) scores. PS396-tau⁺ RGCs in the central and mid-periphery showed the closest associations with disease status, while Oligo-tau⁺ RGCs in the mid-periphery exhibited the strongest correlations with brain pathology (NFTs, Braak stages, ABC scores; $r_s = 0.78$ – 0.81 , $P < 0.001$ – 0.0001) and cognitive decline (MMSE; $r_s = -0.79$, $P = 0.0019$). Overall, these findings identify a link between pathogenic tau in RGCs and RGC degeneration in AD, involving apoptotic and GVD-necroptotic cell death pathways. Future research should validate these results in larger and more diverse cohorts and develop RGC tauopathy as a potential noninvasive biomarker for early detection and monitoring of AD progression.

Keywords Alzheimer's disease, Eye, Tau protein, Amyloid beta, Ganglion cell layer, Retinal ganglion cells

*Correspondence:

Maya Koronyo-Hamaoui
maya.koronyo@csmc.edu

Full list of author information is available at the end of the article



© The Author(s) 2025. **Open Access** This article is licensed under a Creative Commons Attribution 4.0 International License, which permits use, sharing, adaptation, distribution and reproduction in any medium or format, as long as you give appropriate credit to the original author(s) and the source, provide a link to the Creative Commons licence, and indicate if changes were made. The images or other third party material in this article are included in the article's Creative Commons licence, unless indicated otherwise in a credit line to the material. If material is not included in the article's Creative Commons licence and your intended use is not permitted by statutory regulation or exceeds the permitted use, you will need to obtain permission directly from the copyright holder. To view a copy of this licence, visit <http://creativecommons.org/licenses/by/4.0/>.

Introduction

Alzheimer's disease (AD), the most prevalent and progressive form of senile dementia, affects an estimated 6.9 million Americans aged 65 and older [1]. It is characterized by the accumulation of amyloid beta-protein (A β) deposits and abnormal tau protein aggregates in the brain [18, 51]. During AD progression, microtubule-associated tau proteins undergo hyperphosphorylation (p-tau) and form toxic oligomers that spread between neurons, accelerating disease progression [14, 41, 42, 55, 59, 67]. These tau species eventually aggregate into neurofibrillary tangles (NFTs) [82], disrupting cellular functions and axonal transport, which leads to synaptic dysfunction and neuronal death [86, 99, 109, 123]. The presence of abnormal tau strongly correlates with the progression of neurodegeneration and cognitive deficits in AD [20, 37, 41, 52, 68]. AD neuropathology develops many years before neurobehavioral and cognitive disturbances become salient [52, 114, 115, 132]. Therefore, early identification of AD pathological hallmarks in the central nervous system (CNS) is crucial for early intervention and disease management.

The retina, a posterior neurosensory eye tissue, is an extension of the brain and shares many structural and functional features. Recent studies have revealed the genetic basis for eye-brain connections, suggesting bidirectional genetic causal links between retinal structures and neurological disorders, including AD [34, 97, 135]. Growing evidence indicates the presence of AD-related pathological features in the retinas of patients with mild cognitive impairment (MCI due to AD) and/or AD dementia, including various abnormal A β and tau species, vascular damage, micro- and macro-gliosis, and neurodegeneration [2, 5, 7, 8, 16, 17, 22, 28, 30–32, 38, 40, 43, 46, 48, 63–65, 70, 73, 74, 84, 88, 89, 98, 107, 108, 110–112, 118, 129, 131]. Regarding tauopathy, a wide range of abnormal tau isoforms have been identified in the retinas of AD patients, including pretangles and mature tangle forms: 3- and 4-repeat tau, p-tau, and citrullinated tau forms, oligomeric tau (Oligo-tau), paired helical filaments of tau (PHF-tau), as well as paperclip folding of tau and NFT-like structures [28, 30, 40, 45, 46, 63, 89, 112, 129]. We recently found that the retinas of patients with MCI (due to AD) and/or AD dementia exhibit significant increases in pathogenic p-tau at specific epitopes, including S202/T205, S214, S396, S404, and T231, as well as citrullinated R209-tau and tau oligomers (T22-positive), alongside PHF⁺ and MC-1⁺ pretangle and mature tau tangles. Epitopes S199 and T212/S214 did not show similar changes [112]. In particular, Oligo-tau and pS396-tau isoforms, commonly elevated in AD brains [100, 127], were consistently increased in MCI and AD retinas and were strongly associated with more severe brain pathology, advanced disease stages, and cognitive decline [112].

However, the impact of AD-related tauopathy on specific retinal cell types in these patients has yet to be described.

Retinal ganglion cells (RGCs) are neurons located in the retinal ganglion cell layer (GCL; as seen in optical coherence tomography – OCT imaging) and exist in various subtypes, such as midget, parasol, bistratified, and melanopsin-containing intrinsically photosensitive RGCs (mRGCs). These cells serve diverse functions, including high spatial frequency resolution, color differentiation, low spatial frequency contrast, and photoentrainment of the hypothalamus, which regulates circadian rhythms [106, 128]. Dendritic protrusions from the RGC soma receive synaptic input from the axons of bipolar and amacrine cells in the inner plexiform layer (IPL). The RGCs project their axons to form the nerve fiber layer (NFL), which converges at the optic discs and continues as the optic nerve. This pathway ultimately transmits all visual information to the brain [56]. Notably, RGCs, located on the inner retinal surface, are uniquely positioned as neurons in the CNS that can be noninvasively imaged and quantitatively assessed in vivo with high resolution using advanced adaptive optics (AO)-OCT technology, as demonstrated in recent studies [44, 79]. This advanced imaging capability enables a detailed examination of RGC pathology and may facilitate future AD diagnosis and monitoring.

In the context of AD, pioneering studies have demonstrated the loss of RGCs in patients [15, 16, 48]. Other reports have shown visual dysfunctions, such as impaired contrast sensitivity, abnormal color discrimination, and diminished visual fields, which can be attributed to RGC degeneration [38, 54, 101, 104, 125]. Subsequent investigations into the AD retina have found thinning of the NFL, reduced density of melanopsin-containing RGCs, GCL cell loss, and elevated apoptotic markers, along with intraneuronal A β oligomers and other A β species within RGCs in these patients [5–7, 23, 26, 38, 57, 63, 64, 69, 70, 73, 77]. A recent report in several transgenic murine models of AD showed RGC susceptibility, manifested as a reduction in RGC dendritic fields, occurring in parallel with hippocampal dendritic spine loss [13]. An additional study detected an increased total tau burden in RGCs in an AD-murine model [24]. However, the vulnerability of RGCs to pathogenic tau accumulation in AD patients, particularly during the earliest stages of functional impairment (MCI due to AD), and its potential relationship with disease status, has not yet been explored.

In the current study, we addressed these gaps by investigating the density, size, and distribution of RGCs in the superior temporal retinal tissues from patients with MCI (due to AD) and AD dementia, compared with cognitively normal (CN) individuals. We examined whether RGCs in AD express markers of apoptosis, granulovacuolar degeneration (GVD) bodies, and GVD-associated

necroptosis. In addition, we explored whether AD-related pathogenic tau forms, pS396-tau and Oligo-tau, are specifically present within RGCs, and quantified RGCs containing these abnormal tau isoforms in this cohort. The interplay between RGC integrity and pS396-tau- and Oligo-tau-containing RGCs, as well as the overall burden of A β and tau pathology in the retina, was assessed, and correlations with disease status were determined. Our analyses indicated an early and substantial decline in RGCs, which was associated with increased pS396-tau- and Oligo-tau-laden RGCs in MCI and AD patients compared to age- and sex-matched CN controls. RGCs in AD patients exhibited hypertrophic soma and nucleus displacement, concomitant with expression of apoptotic and GVD/necroptotic markers. The levels of pS396-tau- and Oligo-tau-laden RGC counts strongly correlated with corresponding brain pathology and cognitive status.

Materials and methods

Postmortem eyes

Human eye and brain tissues were collected from donor patients with premortem clinical diagnoses of MCI and AD dementia (confirmed by postmortem AD neuropathology), along with age- and sex-matched CN controls (total $n=41$ subjects). These tissues were primarily obtained from the Alzheimer's Disease Research Center (ADRC) Neuropathology Core in the Department of Pathology (IRB protocol HS-042071) at the Keck School of Medicine, University of Southern California (USC, Los Angeles, CA). Additional eyes were obtained from the National Disease Research Interchange (NDRI, Philadelphia, PA) under the approved Cedars-Sinai Medical Center IRB protocol Pro00019393. Both USC-ADRC

and NDRI maintain human tissue collection protocols approved by their managerial committees and subject to oversight by the National Institutes of Health. Histological studies at Cedars-Sinai Medical Center were performed under IRB protocols Pro00053412 and Pro00019393. Demographic, clinical, and neuropathological information on human donors is detailed in Tables 1 and Suppl. Table 1. Subjects with macular degeneration, glaucoma, and diabetic retinopathy were excluded from this study. The available retinal tissues from individual donors are specified in Suppl. Table 1. For the histopathological analysis, the human cohort consisted of AD dementia ($n=15$), MCI due to AD ($n=10$), and CN controls ($n=16$). All patients' identities were protected by de-identifying tissue samples, ensuring they could not be traced back to the donors.

Clinical and neuropathological assessments

The ADRC provided clinical and neuropathological reports on patients' neurological examinations, neuropsychological and cognitive tests, family history, and medication lists, as collected in the ADRC system using the Uniform Data Set (UDS) [12]. The NDRI provided the medical history of additional patients. Most cognitive evaluations were performed annually and, in most cases, less than one year prior to death. Cognitive testing scores from evaluations made closest to the patient's death were used for this analysis. Two global indicators of cognitive status were used for clinical assessment: the Clinical Dementia Rating (CDR scores: 0 = normal; 0.5 = very mild impairment; 1 = mild dementia; 2 = moderate dementia; or 3 = severe dementia) [85] and the Mini-Mental State Examination (MMSE scores: 24–30 = CN; 20–23 = MCI;

Table 1 Demographic and neuropathological data on human brain and retinal donors in this study

	CN	MCI	AD	F	P
Retinal samples ($N=41$)	16 10 F (63%) 6 M	10 7 F (70%) 3 M	15 8 F (53%) 7 M	-	-
Age at death (years)	80.5 \pm 11.1	88.4 \pm 6.6	87.5 \pm 8.0	2.93	0.07
Race	14 W, 1 H, 1 B	8 W, 1 B, 1 H	12 W, 2 H, 1 A	-	-
PMI (h)	7.8 \pm 4.5	10.1 \pm 5.4	8.8 \pm 4.5	0.5	0.73
MMSE score ($N=30$)	28.7 \pm 2.1	20.1 \pm 7.0	13.8 \pm 7.3	17.01	<0.0001
CDR score ($N=31$)	0.57 \pm 0.8	2.1 \pm 1.1	2.5 \pm 0.9	10.53	0.0004
Brain neuropathology ($N=32$)	Braak stage (%)			15.2	<0.0001
		0-II (57%)	0-II (30%)	0-II (0%)	
		III-IV (43%)	III-IV (30%)	III-IV (13%)	
		V-VI (0%)	V-VI (40%)	V-VI (87%)	
	ABC average	1.37 \pm 0.91	2.20 \pm 0.59	2.82 \pm 0.21	17.13
A β plaque (severity score)	1.12 \pm 1.31	1.88 \pm 0.79	2.65 \pm 0.77	6.98	0.0034
NFTs (severity score)	0.43 \pm 0.53	1.71 \pm 0.91	2.36 \pm 0.70	16.06	<0.0001
NTs (severity score)	0.49 \pm 0.99	1.24 \pm 0.82	1.69 \pm 0.90	4.27	0.024

List of human donors included in this study ($N=41$ subjects). Paired brains with neuropathological assessments were available for 32 human donors. ABC scores comprise of mean grades for: (A) A β plaque score modified from Thal, (B) NFT stage modified from Braak, and (C) neuritic plaque score modified from CERAD. Group values are presented as mean \pm standard deviation. F and P -values were determined using one-way analysis of variance (ANOVA) with Tukey's multiple comparisons test. P -values presented in bold type demonstrate statistical significance. Abbreviations: A β , amyloid beta-protein; AD, Alzheimer's disease; A, Asian; B, Black; CDR, Clinical Dementia Rating; CN, cognitively normal controls; F, female; H, Hispanic; M, male; MCI, mild cognitive impairment; MMSE, Mini-Mental State Examination; NFTs, neurofibrillary tangles; NTs, neuropil threads; PMI, postmortem interval; W, White

10–19 = moderate dementia; or $9 \geq$ severe dementia) [35]. In this study, the composition of the clinical diagnostic groups (AD, MCI, or CN) was determined by source clinicians based on a comprehensive battery of tests, including neurological examinations, neuropsychological evaluations, and the cognitive tests. Specifically, the diagnosis of MCI due to AD was assigned to patients who had an antemortem clinical diagnosis of MCI (based on the comprehensive battery of behavioral and cognitive tests) caused by AD. These patients had a postmortem confirmation of AD neuropathology (according to the ADNC—Alzheimer’s disease neuropathological change guidelines) and showed no evidence of other diseases, such as Lewy body dementia, Parkinson’s disease, FTD/FTLD (PSP or Pick’s disease), or cognitive impairment due to stroke or small vessel disease.

To obtain a final diagnosis based on the neuropathological reports, we used the modified Consortium to Establish a Registry for Alzheimer’s Disease (CERAD) criteria [80, 103], as outlined in the National Institute on Aging (NIA)/Regan protocols with revisions by the NIA and Alzheimer’s Association [50]. The assessment included A β burden (measured as diffuse, immature, or mature plaques), amyloid angiopathy, neuritic plaques, NFTs, neuropil threads (NTs), granulovacuolar degeneration, Lewy bodies, Hirano bodies, Pick bodies, balloon cells, neuronal loss, microvascular changes, and gliosis. These pathologies were assessed in multiple brain areas, including the hippocampus (particularly the Cornu ammonis CA1, at the level of the thalamic lateral geniculate body), entorhinal cortex, superior frontal gyrus of the frontal lobe, superior temporal gyrus of the temporal lobe, superior parietal lobule of the parietal lobe, primary visual cortex (Brodmann Area-17), and visual association (Area-18) of the occipital lobe. In all cases, uniform brain sampling was conducted by a neuropathologist.

Cerebral amyloid plaques, NFTs, and NTs were evaluated using anti- β -amyloid mAb clone 4G8 immunostaining, Thioflavin-S (ThioS) histochemical staining, and Gallyas silver staining in formalin-fixed, paraffin-embedded tissue sections. The ADRC neuropathologists assigned severity scores based on semi-quantitative observations. The scale for A β /neuritic plaques was determined by the presence of 4G8- and/or Thioflavin-S-positive and/or Gallyas silver-positive plaques measured per 1 mm² of brain area (0 = none; 1 = sparse [≤ 5 plaques]; 3 = moderate [6–20 plaques]; 5 = abundant/frequent [21–30 plaques or greater]; or N/A = not applicable), as previously described [83] in the NACC NP Guidebook, Version 10, January 2014: <https://naccdata.org/data-collection/forms-documentation/np-10>. The brain NFT or NT severity scoring system was derived from observed burden of these AD neuropathologic changes, as detected by Gallyas silver and/or Thioflavin-S

staining [82, 83, 126], and measured per 1 mm² of brain area. The assigned NFT or NT scores were as follows: 0 = none; 1 = sparse (mild burden); 3 = moderate (intermediate burden); or 5 = frequent (severe burden). For both histochemical and immunohistochemical staining, each anatomical area of interest was assessed for relevant pathology using a 20X objective (200X high power magnification), and representative fields were graded using the semiquantitative scale as detailed above. Validation of AD neuropathic change (ADNC), especially NTs, was performed using a 40X objective (400X high power magnification), and an average of two readings was assigned to each individual patient.

A final diagnosis of AD neuropathological change was determined using an “ABC” score derived from three separate 4-point scales. We used the modified A β plaque Thal score (A0 = no A β or amyloid plaques; A1 = Thal phase 1 or 2; A2 = Thal phase 3; or A3 = Thal phase 4 or 5) [122]. For the NFT stage, we applied the modified Braak staging for silver-based histochemistry or p-tau IHC (B0 = no NFTs; B1 = Braak stage I or II; B2 = Braak stage III or IV; or B3 = Braak stage V or VI) [19]. For neuritic plaques, we used the modified CERAD score (C0 = no neuritic plaques; C1 = CERAD score sparse; C2 = CERAD score moderate; or C3 = CERAD score frequent) [80]. Neuronal loss, gliosis, granulovacuolar degeneration, Hirano bodies, Lewy bodies, Pick bodies, and balloon cells were all evaluated (0 = absent; 1 = present) in multiple brain areas by staining tissues with hematoxylin and eosin (H&E). Brain atrophy was evaluated (0 = none; 1 = mild; 3 = moderate; 5 = severe; or 9 = not applicable).

Processing of eye globes and retinal tissues

The processing of eye globes, isolation and preparation of retinal strips, and retinal immunostaining were extensively detailed in [63, 64, 112]. Briefly, donor eyes were collected within an average of 9 h after death, puncture at the limbus and fixed in 10% neutral buffered formalin (NBF) or 4% paraformaldehyde (PFA) then stored at 4 °C. Regardless of the source of the human donor eye (USC-ADRC or NDRI), the same tissue collection and processing methods were applied.

Preparation of retinal strips

Eyes fixed in 10% NBF or 4% PFA were dissected as previously described [63, 64, 112]. Flatmounts were prepared after careful dissection of the eye globes and thorough cleaning of the vitreous humor. Flatmount strips (~2 mm wide) extending diagonally from the optic disc (OD) to the ora serrata (~20–25 mm long) were prepared in 4 predefined regions: Superior Temporal (ST), Inferior Temporal (IT), Inferior Nasal (IN), and Superior Nasal (SN). In this study, we focused our analysis on the ST retinal strip due to the high presence of AD pathology

in this region [63, 64, 112]. The flatmount-derived strips were then paraffinized using standard techniques and embedded in paraffin after flip-rotating 90° horizontally. The retinal strips were sectioned (7–10 µm thick) and mounted on microscope slides coated with (3-Aminopropyl) triethoxysilane. This sample preparation technique allowed for extensive and consistent access to retinal quadrants, layers, and pathological subregions.

Immunofluorescent staining

Retinal sections were deparaffinized using 100% xylene twice (10 min each), rehydrated with decreasing concentrations of ethanol (100–70%), and washed with distilled water followed by PBS. After deparaffinization, tissue sections were treated with target retrieval solution (pH 6.1; S1699, Dako) at 98 °C for 1 h and then washed with PBS. Next, tissues were incubated in blocking buffer (Dako #X0909) supplemented with 0.1% Triton X-100 (Sigma, T8787) for 1 h at room temperature (RT), followed by overnight incubation with primary antibody (Ab) at 4 °C (Abs information provided in Suppl. Table 2). The sections were then washed three times with PBS and incubated with secondary Abs against each species (1:200, Suppl. Table 2) for 1 h at RT. After rinsing with PBS three times, the sections were mounted with Pro-Long Gold antifade reagent with DAPI (Thermo Fisher #P36935).

Peroxidase-based immunostaining

After deparaffinization and antigen retrieval treatment, the tissues were treated with 70% formic acid (ACROS) for 10 min at room temperature. The tissues were then washed with wash buffer (Dako S3006) supplemented with 0.1% Triton X-100 (Sigma, T8787) for 1 h, followed by treatment with H₂O₂ for 10 min and a rinse with wash buffer. Primary Ab (Suppl. Table 2) were diluted with background reducing components (Dako S3022) and incubated with the tissues overnight at 4 °C. The tissues were rinsed thrice with wash buffer on a shaker and incubated for 30 min at 37 °C with secondary Ab (goat anti-rabbit HRP conjugated, Dako Envision K4003), followed by three more rinses with wash buffer on a shaker. Diaminobenzidine (DAB) substrate (Dako K3468) was then applied. Some slides were counterstained with hematoxylin and mounted with Faramount aqueous mounting medium (Dako, S3025). Routine controls were processed using an identical protocol, while omitting the primary antibodies to assess nonspecific labeling.

Nissl staining

A basic (alkaline) dye was used to label nuclei and granules (i.e., ribosomal RNA) in neurons. The cytoplasm of neurons is specifically stained with the Nissl staining technique, while the perikarya of other cellular elements

are either weakly visualized or not at all [53]. Deparaffinized and rehydrated sections were stained in 0.1% Cresyl Violet acetate (Sigma #C5042) for 5 min, rapidly rinsed in tap water, and briefly dipped in 70% ethanol. The sections were then dehydrated through 2 changes of absolute ethanol for 3 min each, followed by immersion in xylene twice for 2 min and mounted in mounting medium xylene (Fisher scientific company, L.L.C. #245–691). An average of 12 images (from the superior quadrant), covering the retinal neurons from the optic disc to the ora serrata, were captured at a 20x objective and analyzed to quantify the area and number of retinal GCL neurons.

Microscopy and stereological quantification

Fluorescence and brightfield images were acquired using a Carl Zeiss Axio Imager Z1 fluorescence microscope (with motorized Z-drive) equipped with Apo-Tome, AxioCam HRc, and AxioCam MRm monochrome cameras (version 3.0; resolution of 1388×1040 pixels, 6.45 µm × 6.45 µm pixel size, and a dynamic range of >1:2200, which delivers low-noise images due to a Peltier-cooled sensor) with ZEN 2.6 blue edition software (Carl Zeiss MicroImaging, Inc.). Multi-channel image acquisition was used to create images with multiple channels. Images were consistently captured at the same focal planes with identical exposure time, using a 20x objective at a resolution of 0.25 µm. Approximately 15 images were obtained from each retina. The acquired images were converted to grayscale and standardized to baseline using a histogram-based threshold in Fiji ImageJ (NIH) software (version 1.53c). For each biomarker, the total area of immunoreactivity was determined using the same threshold percentage from the baseline in ImageJ (with the same percentage threshold setting for all diagnostic groups). The images were then subjected to particle analysis to determine the immunoreactive (IR) area and/or area fraction (%). For each immunoreactivity quantification, all slides and microscopic images were processed and acquired in a single batch.

RGC soma size measurement

The size of RGC somas was measured using Fiji ImageJ (NIH) software (version 1.53c) with the polygonal selection tool. For each 20x retinal image (10–12 images per patient), the soma area of the top 3 largest RBPMS⁺ RGCs was measured; 30–36 RGCs per patient were analyzed. In addition, all identifiable RBPMS⁺ RGCs were manually assessed in each field throughout the entire retinal strips (a total of 2,051 cells). RGC soma area measurements of all cells and the average RGC soma area per patient, across all retinal subregions, were plotted for each diagnostic group and subjected to statistical analysis.

Statistical analysis

GraphPad Prism Software version 9.5.1 was used for statistical analyses. One-way or two-way ANOVA followed by Tukey's multiple comparison post-test was used to determine statistical significance between three or more groups. Two-group comparisons were analyzed using a two-tailed unpaired Student's *t*-test. The statistical association between two variables was determined by Pearson's correlation (parametric) or Spearman's rank correlation (non-parametric) analyses. Pair-wise Pearson's (r_p) or Spearman's (r_s) coefficients, with unadjusted *P* values, were used to indicate the direction and strength of the linear relationship between the two variables. Results are expressed as the mean \pm standard deviation (SD) in tables, as median, lower, and upper quartiles in violin plots and mean \pm standard error of the mean (SEM) in bar graphs. Degrees of significance are presented as: * $P < 0.05$, ** $P < 0.01$, *** $P < 0.001$, and **** $P < 0.0001$. Data analysis was conducted using coded identifiers, and analysts remained blinded to the diagnostic groups until all analyses were completed.

Results

We investigated the integrity of RGCs, including their number, morphology, and distribution, in relation to abnormal retinal tau isoforms and their accumulation within RGCs in early and advanced-stage AD. Retinal superior temporal (ST) cross-sections (Fig. 1a, b) were analyzed from MCI due to AD ($n = 10$, mean age 88.4 ± 6.6 years, 7 females/3 males), AD dementia ($n = 15$, mean age 87.5 ± 8.0 years, 8 females/7 males), and CN controls ($n = 16$, mean age 80.5 ± 11.1 years, 10 females/6 males). Demographic, clinical, and neuropathological information is detailed in Table 1 (list of individual donor eyes and respective brains detailed in Suppl. Table 1).

RGC loss and apoptosis in MCI and AD patients

We first assessed RGC numbers and distribution across ST subregions in a sub-cohort of patients with MCI ($n = 6$, mean age 89.5 ± 5.24 years, 3 females/3 males), AD ($n = 10$, mean age 86.0 ± 8.89 years, 4 females/6 males), and age- and sex-matched CN controls ($n = 9$, mean age 85.89 ± 11.85 years, 5 females/4 males), using a selective pan-RGC marker, ribonucleic acid binding protein with multiple splicing (RBPMS), for immunohistochemical (IHC) analysis. Previous studies have shown that, RBPMS is specifically expressed in the entire RGC population, despite the heterogeneity of other neurons under pathological conditions, including displaced amacrine cells within the GCL [91, 94, 102]. Compared to the retinas of CN individuals, the density of RGCs appeared lower in MCI and AD dementia patients, with their cytoplasm enlarged or swollen (Fig. 1c; extended data for RBPMS with DAPI nuclei staining in Suppl. Figure 1a).

Quantitative analysis of RBPMS⁺ RGC counts per retinal subregion (central, mid-, and far-periphery) and the total ST region revealed substantial reductions in RGC count and percent area—ranging from 42–65%—in MCI and AD patients compared to CN individuals (Fig. 1d, e and Suppl. Figure 1b; $P < 0.05 - 0.01$). RBPMS⁺ RGC count loss in MCI and AD retinas was more significant in the mid- and far-periphery regions, which are distal from the optic nerve head.

We next examined neurodegeneration in the GCL using Nissl staining, an alkaline dye that labels nuclei and granules (i.e., ribosomal RNA) in neurons, in a sub-cohort of patients diagnosed with MCI ($n = 10$, mean age 88.4 ± 6.6 years, 7 females/3 males), AD ($n = 15$, mean age 87.5 ± 8.0 years, 8 females/7 males), and CN controls ($n = 14$, mean age 80.6 ± 12.1 years, 9 females/5 males) (Fig. 1f-i). Representative images from the central ST region showed a reduction in cell numbers across all retinal layers (Fig. 1f), particularly in the GCL (Fig. 1g), in MCI and AD patients compared to CN controls. Quantitative analysis of Nissl⁺ percent area in the GCL across retinal subregions indicated a marked 53-64% neuronal loss in the central and mid-peripheral subregions of MCI and AD patients compared to CN controls (Suppl. Figure 1c). No statistically significant reduction was observed in the far-peripheral subregion. In the total ST region, a substantial 55-56% reduction in Nissl⁺ percent area in the GCL was observed for both AD and MCI groups compared to CN controls (Fig. 1h; $P < 0.01 - 0.001$). Pearson's correlation coefficient (*r*) analysis demonstrated a strong correlation between the two RGC integrity parameters, RBPMS⁺ RGCs and Nissl⁺ GCL residing neurons percent areas ($r = 0.63$, $P = 0.0011$; Fig. 1i). To assess whether RGCs or GCL residing neurons were lost due to apoptotic cell death mechanisms, we performed IHC using an antibody against an early apoptotic marker [124], cleaved caspase 3 (CCasp3; Fig. 1j-l). Increased CCasp3 labeling was observed in RBPMS⁺ RGCs of MCI and AD patients (Fig. 1j; extended data in Suppl. Figure 1d). Quantitative analysis of percent CCasp3⁺ GCL residing cells revealed a significant 1.5-fold and 1.3-fold increase in AD retinas compared to CN and MCI retinas, respectively (Fig. 1k; $P < 0.05 - 0.01$), with no differences noted between MCI and CN retinas. Similarly, a quantitative analysis of colocalized CCasp3⁺RBPMS⁺ RGC count showed a significant 1.8-fold increase in AD compared to MCI and CN groups (Suppl. Figure 1e; $P < 0.05$). Notably, the percent of CCasp3⁺RBPMS⁺ RGCs of the total RBPMS⁺ cell population was markedly increased by 2.8-fold in AD compared to CN, with a non-significant trend of increase in the MCI group (Fig. 1l; $P < 0.001$). This analysis showed that compared to ~10% RGC-expressing CCasp3 in CN individuals, this number was elevated to approximately 25–30% apoptotic RGCs in MCI and AD patients (Fig. 1l;

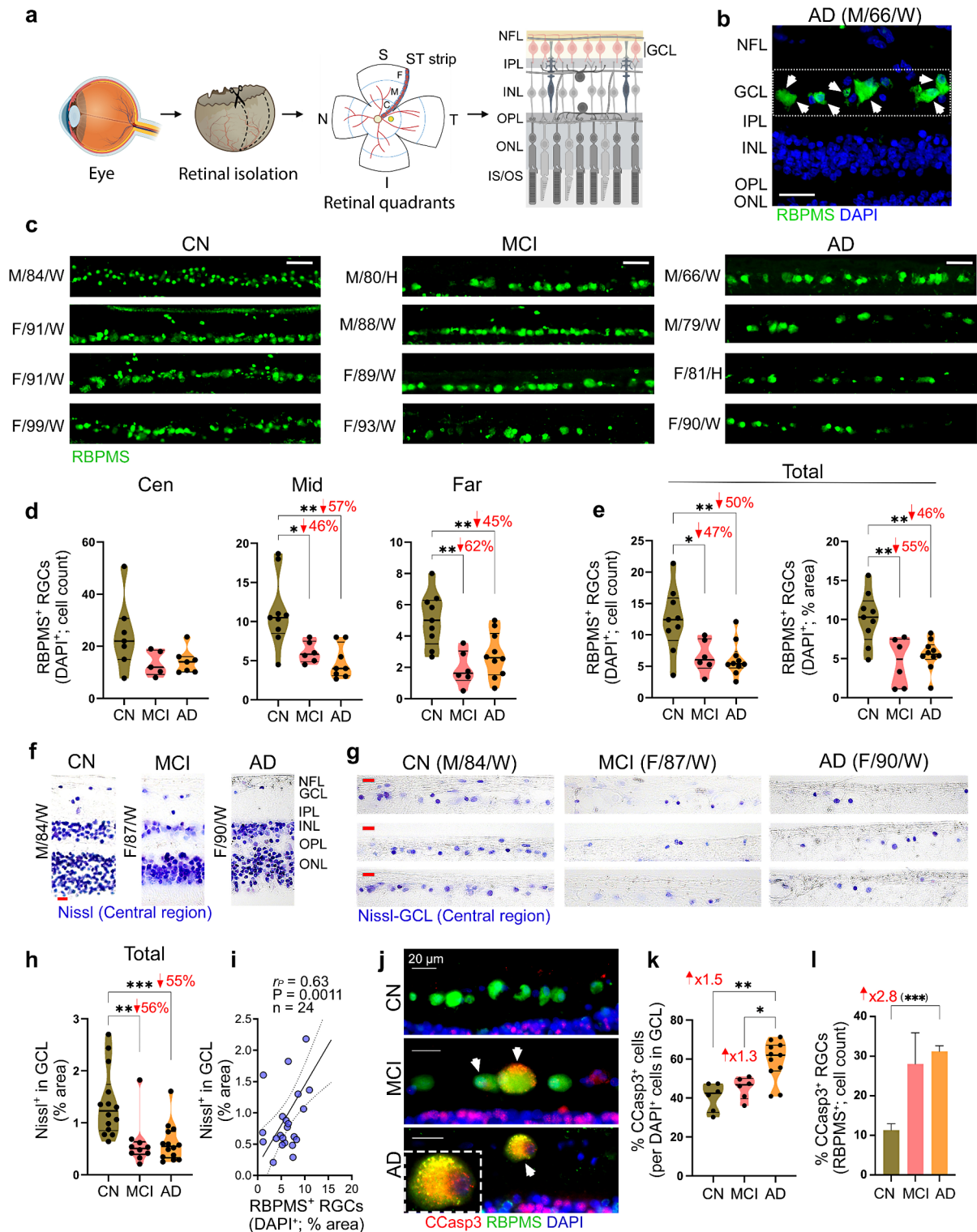


Fig. 1 (See legend on next page.)

(See figure on previous page.)

Fig. 1 Ganglion cell integrity in retinal tissues of MCI and AD patients. **(a)** Illustration of the histological process, including retinal isolation, cross-section preparation, and analysis of the superior temporal (ST) strip, extending from the optic disc to the ora serrata and anatomically predefined into central (Cen, C), middle (Mid, M) and far-peripheral (Far, F) subregions. The retinal ganglion cell layer (GCL) was analyzed in this study. **(b)** Microscopic image of a retinal cross-section from an AD patient, immunolabeled with retinal ganglion cell (RGC)-specific marker, ribonucleic acid binding protein with multiple splicing (RBPMS; green), and nuclei labelling with DAPI (blue). Scale bar: 25 μm . **(c)** Representative microscopic images of RGCs within the GCL, labeled with RBPMS (green), in retinal cross-sections from patients with mild cognitive impairment (MCI due to AD, $n=4$) and Alzheimer's disease (AD) dementia ($n=4$), and cognitively normal individuals (CN, $n=4$). Scale bar: 50 μm . **(d, e)** Violin plots display quantitative immunohistochemistry analyses of RBPMS⁺DAPI⁺ RGCs by **(d)** cell count in Cen, Mid- and Far-peripheral subregions, and **(e)** cell count (left) and percent area (right) in the total ST region ($n=25$ subjects; $n=9$ CN, $n=6$ MCI, $n=10$ AD). **(f, g)** Representative microscopic images of retinal cross-sections from CN, MCI, and AD donors labeled with Nissl (purple) in **(f)** all analyzed retinal layers (ONL to NFL) and **(g)** GCL separately, in the Central ST subregion. Scale bars: 20 μm . **(h)** Quantitative analyses of Nissl⁺ percent area in the GCL for the total ST region ($n=38$ subjects; $n=14$ CN, $n=10$ MCI, $n=14$ AD). **(i)** Pearson's correlation coefficient (r_p) analysis between RBPMS⁺ RGCs percent area and Nissl⁺ cells (in GCL) percent area. **(j)** Representative microscopic images of the early apoptotic cell marker, cleaved caspase-3 (CCasp3⁺, red) in RBPMS⁺ cells (green) with nuclei DAPI (blue) in the GCL of CN, MCI and AD donors. **(k)** Quantitative analysis of the percent area of CCasp3⁺ in the GCL, normalized to nuclei count ($n=23$ subjects; $n=6$ CN, $n=6$ MCI, $n=11$ AD). **(l)** Percentage of CCasp3⁺RBPMS⁺ RGC count in a subset of the same cohort. The bar graph displays mean \pm SEM. Violin plots show individual data points and median, lower, and upper quartiles. * $P<0.05$, ** $P<0.01$, *** $P<0.001$, **** $P<0.0001$, by one-way or two-way ANOVA followed by Tukey's post-hoc multiple comparison test or unpaired Student t-test (in parenthesis). Percent decreases and fold changes are shown in red. F, female; M, male; Age (in years); Ethnicity: W, White and H, Hispanic; NFL, Nerve fiber layer; IPL, Inner Plexiform Layer; INL, Inner Nuclear Layer; OPL, Outer Plexiform Layer; ONL, Outer Nuclear Layer; IS/OS, inner segment and outer segment. Illustrations created with Biorender.com

Extended data on retinal CCasp3 immunoreactive area normalized to retinal thickness showed significant 1.5- and 3.1-fold increases in MCI and AD, respectively, as compared to CN (Suppl. Figure 1f; $P<0.05$ and <0.0001 , respectively).

RGC hypertrophy and GVD-associated necroptosis

We next analyzed the morphological changes in RGCs of MCI and AD patients compared to CN controls (Fig. 2a, b). We found that RGCs in MCI and AD patients often exhibited a hypertrophic cell soma, with nucleus displacement, and patterns of granulovacuolar degeneration (GVD)-like bodies, as indicated by red and white arrows, respectively (Fig. 2a). Quantitative analysis of the largest RBPMS⁺ ganglion cells, across the central, mid- and far-peripheral ST retina, revealed a significant 1.5-fold enlargement of the granulomatous soma-cell area in AD patients compared to CN controls (Fig. 2c; $P<0.05$), with no significant change observed in the MCI group. Due to the highly diverse population of RGCs [56], we also performed an extensive quantification of all identifiable RBPMS⁺ RGC soma size (a total of 2,051 cells), across the ST retina (Fig. 2d) and in the central, mid-periphery, and far-periphery subregions (Fig. 2e-g). This analysis indicated significant 1.1-1.3-fold increases of RGC-soma area in MCI and AD relative to CN ($P<0.05$ - $P<0.0001$). RGC hypertrophy was highly significant in the central and mid-peripheral subregions (Fig. 2e, f). No significant RGC-soma area increase was observed in the far-periphery subregion (Fig. 2g). The observation of GVD-like punctate staining patterns in RBPMS⁺ RGCs of MCI and AD patients prompted us to investigate whether markers of GVD and GVD-associated activation of the necroptosis pathway (GVD-necroptosis) were present in these cells (Fig. 2h, i). Immunohistochemistry of the GVD marker, charged multivesicular body protein 2B (CHMP2B), commonly detected in brain neuronal

GVDs [130], revealed prominent CHMP2B expression in RBPMS⁺ RGCs of MCI and AD patients, including in hypertrophic RGCs (Fig. 2h, white arrows). Furthermore, immunolabeling for the GVD-associated activation of necroptosis pathway (GVD-necroptosis) marker, phosphorylated mixed lineage kinase domain-like (pMLKL) [60, 61] confirmed the presence of pMLKL GVD-necroptotic proteins within RBPMS⁺ RGCs of MCI and AD patients (Fig. 2i, white arrows).

Increased pS396-tau and oligo-tau in RGCs linked to RGC depletion

We recently reported significant increases in abnormal tau isoforms, particularly pretangle forms such as pS396-tau and Oligo-tau, in the retina of MCI and AD patients [112]. Here, we investigated whether RGCs are vulnerable to the accumulation of these pretangle (pS396-tau and Oligo-tau) and mature tangle (PHF-tau) isoforms in early and advanced AD patients (Figs. 3 and 4; extended data in Suppl. Figure 2 and Suppl. Figure 3). First, we performed IHC analysis employing antibody combinations of RBPMS with PHF-1 (Fig. 3a) and PHF-1 with pS396 (Fig. 3b). The pS396 antibody detects tau phosphorylated at serine 396, while the PHF-1 antibody recognizes pS396- and pS404-tau in paired helical filaments. We found that PHF-tau was rarely observed within the soma of RBPMS⁺ RGCs, and most RGCs were PHF-tau negative (Fig. 3a, white arrows in lower image). In contrast, pS396-tau was frequently detected within RGCs of MCI and AD patients (Fig. 3b-e). Excluding the RGC soma, both PHF-1 and pS396 colocalized in the inner retinal layers and OPL in MCI and AD patients (Fig. 3b, yellow). Increased pS396-tau burden in the OPL, IPL, GCL, and NFL, accompanied by hypertrophic soma and reduced RBPMS⁺ RGCs, was observed in MCI and AD patients compared to CN controls (Fig. 3c). The three-parallel-string staining pattern of retinal pS396-tau in the

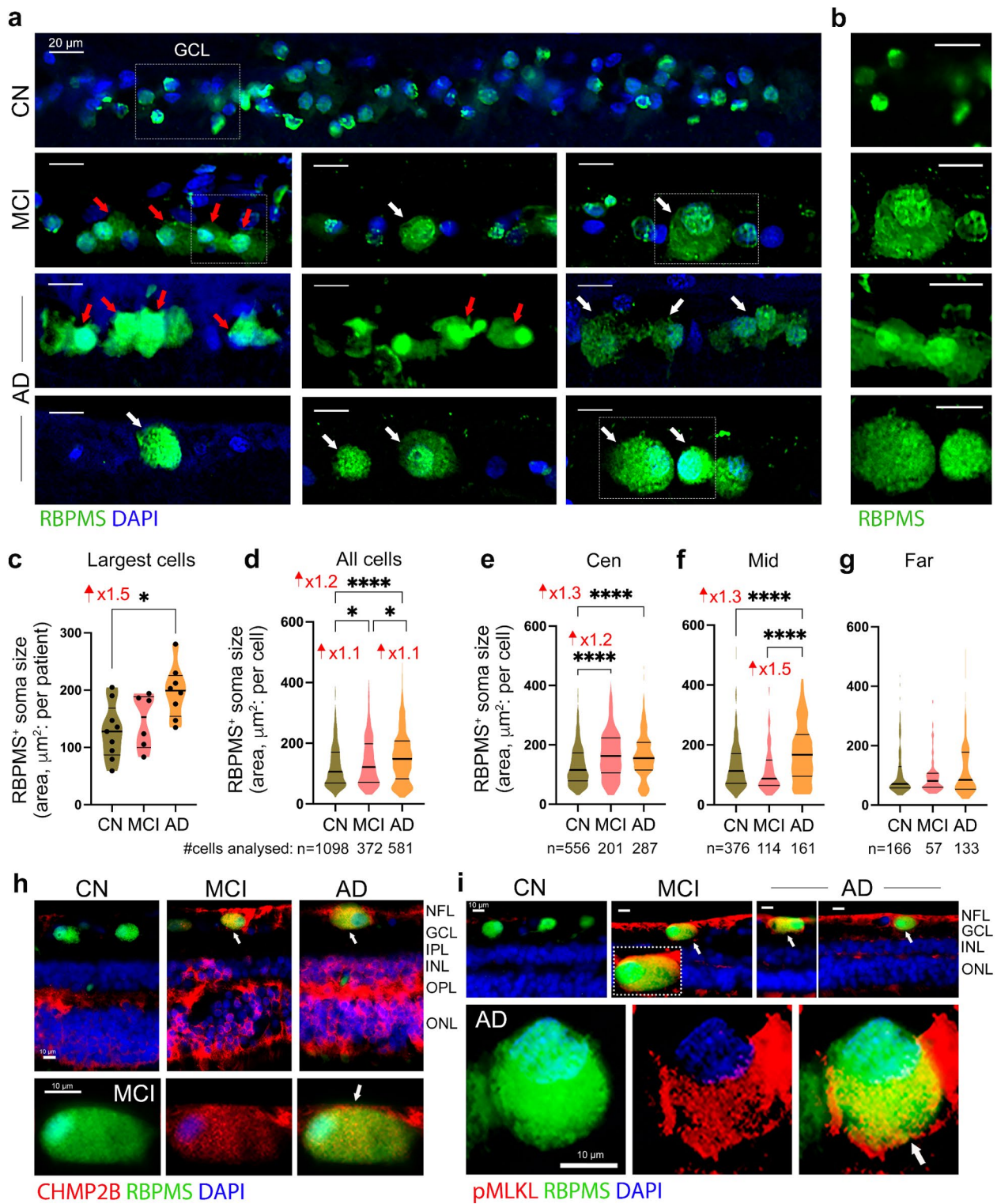


Fig. 2 (See legend on next page.)

(See figure on previous page.)

Fig. 2 RGC hypertrophy and GVD-associated necroptosis in MCI and AD patients. **(a)** Representative microscopic images of retinal cross-section immunofluorescently labeled for RGC-specific marker RBPMS (green) and nuclei (DAPI blue), in the GCL, showing abnormal morphology of RGCs in MCI and AD retinas as compared with CN controls. Retinas from MCI and AD patients exhibit a hypertrophic cytoplasm (cell soma swelling), and abnormal morphology, including granulovacuolar vesicles degeneration (GVD)-like bodies and nucleus displacement. Red arrows point to nuclear displacement and white arrows indicate granulomatous cytoplasm. **(b)** Enlarged images of RBPMS⁺ RGCs (green channel only) in the respective diagnostic groups. Scale bars: 20 μ m. **(c)** Quantitative analysis of RBPMS⁺ RGC soma cell size of the three largest cells per microscopic image, in patients with MCI and AD compared to CN controls. **(d-g)** Quantitative analysis of soma cell size for all RBPMS⁺ RGCs analyzed in total ST region **(d)**, and in Cen **(e)** Mid-**(f)** and Far-**(g)** peripheral subregions, in $n=9$ CN, $n=6$ MCI, $n=10$ AD; total number of cells that were analyzed are indicated below the graphs. **(h)** Representative microscopic images of retinal cross-section immunofluorescently labeled for the GVD marker, charged multivesicular body protein 2B (CHMP2B, red), RBPMS for RGCs (green), and DAPI for nuclei (blue) in CN, MCI, and AD donors. Colocalization of CHMP2B within RBPMS⁺ RGCs (yellow) is indicated by white arrows. Scale bars: 10 μ m. **(i)** Representative microscopic images of retinal cross-section immunolabeled for the GVD-associated necroptotic marker, phosphorylated mixed lineage kinase domain-like (pMLKL, red), RBPMS (green), and DAPI (blue) in CN, MCI, and AD subjects. Colocalization of pMLKL within RBPMS (yellow) is indicated by white arrows. Scale bars: 10 μ m. Individual data points and median, lower, and upper quartiles are shown in violin plots. * $P < 0.05$, **** $P < 0.0001$, by one-way ANOVA followed by Tukey's post-hoc multiple comparison test. Fold changes are shown in red. GCL, Ganglion cell layer; NFL, Nerve fiber layer; IPL, Inner Plexiform Layer; INL, Inner Nuclear Layer; OPL, Outer Plexiform Layer; ONL, Outer Nuclear Layer

IPL of MCI and AD patients appeared to accumulate in the neuronal dendrites of RGCs, connecting with axons of bipolar and amacrine cells. We next immunolabeled retinal cross-sections for pS396-tau in combination with RBPMS and parvalbumin, the latter being a marker of horizontal cells within the OPL and RGCs [58]. This analysis identified pS396-tau accumulation within enlarged RBPMS⁺ RGCs (white arrows) and horizontal cells (yellow arrows) of MCI and AD patients, and occasionally in RBPMS⁺ RGCs of CN individuals (Fig. 3d, e and Suppl. Figure 2a). The pS396-tau buildup within the somas of RGCs in the GCL was also evident in non-fluorescence, peroxidase-based IHC staining (Fig. 3f, red arrows).

Quantitative IHC analysis of retinal pS396-tau⁺ percent area showed highly significant 2.4-fold increases in MCI and AD patients compared to CN controls (Fig. 3g; $p < 0.0001$). Pearson's correlation coefficient (r_p) analysis revealed an inverse correlation between retinal pS396-tau burden and RBPMS⁺ RGC area (Fig. 3h; $r_p = -0.60$ and $P = 0.0017$). Notably, pS396-tau-positive RBPMS⁺ RGC counts were significantly elevated in MCI (2.1-2.3-fold; $P < 0.05 - 0.01$) and further increased in AD (2.9-4.1-fold; $P < 0.01 - 0.0001$) retinas, compared to CN controls, across retinal subregions and in the total ST region (Fig. 3i, j). Increases in pS396-tau⁺ RBPMS⁺ RGC count, as well as the percentage area of pS396-tau⁺ in the GCL of MCI and AD patients, were more significant in the central ST retina (Fig. 3i and Suppl. Figure 2b, c). Elevated retinal pS396-tau was associated with a higher number of pS396-tau-laden RGCs and increased CCasp3 in the GCL (Suppl. Figure 2d, e).

Next, IHC analysis of T22⁺ Oligo-tau in the retina of MCI and AD patients compared to CN controls identified oligo-tau deposition within swollen RBPMS⁺ RGCs (Fig. 4a, white arrows) and prominent Oligo-tau staining in the GCL (Fig. 4b; T22⁺ RGCs are indicated by morphology and location with white arrows). Quantitative analysis of retinal Oligo-tau⁺ percent area confirmed the

substantial 5.6- and 9.6-fold increases in MCI and AD patients, respectively, compared to CN controls (Suppl. Figure 3a; $p < 0.01 - 0.001$). Notably, both Oligo-tau⁺ RGC counts and percent Oligo-tau⁺ RGC population were significantly elevated in MCI and AD (2.0-3.5-fold; $P < 0.05 - < 0.0001$) compared to CN controls in the ST retina (Fig. 4c, d; extended data across retinal subregions in Suppl. Fig. 3b, c). No difference in percent Oligo-tau-laden RGC population was observed between MCI and AD (Fig. 4d), whereas a significant 1.7-fold further increase in Oligo-tau-laden RGC counts was detected in AD dementia compared to the MCI group (Fig. 4c; $P < 0.05$). Similar to pS396⁺ RGCs, increases in Oligo-tau⁺ RGCs in MCI and AD were more pronounced and significant in the central subregion (Suppl. Fig. 3b, c). Concomitant with abnormal tau accumulation in RGCs, we also detected significant increases in intra-RGC scFvA13⁺ A β oligomers and retinal 12F4⁺ A β ₄₂ burden in this cohort of MCI and AD patients versus CN controls (Fig. 4e, f). Interestingly, we found a very strong correlation between pS396- and Oligo-tau laden RGCs (Fig. 4g; $r_p = 0.85$ and $P > 0.0001$).

We further investigated the interrelations between retinal abnormal tau and A β burden, including in RGCs, and RGC integrity, as assessed by Nissl⁺ in GCL and RBPMS⁺ RGCs percent areas (Fig. 4h; extended data in Suppl. Figure 3d-g). Pearson's (r) correlation analysis showed inverse correlations between RGC integrity and retinal A β ₄₂ burden (Fig. 4h and Suppl. Figure 3e; $r_p = -0.53$ and $P = 0.033$), and intraneuronal Oligo-A β in GCL (Fig. 4h and Suppl. Figure 3f; $r_p = -0.74$ and $P = 0.0022$). Notably, we found multiple inverse associations between RGC integrity and pS396-tau and Oligo-tau burden in the retina, and specifically in RGCs (Fig. 4h and Suppl. Figure 3d, g; $r_p = -0.40 - (-0.64)$ and $P < 0.05 - 0.01$). These data suggest that elevated levels of abnormal pretangle tau forms in the retina, including within RGCs, are linked to RGC loss.

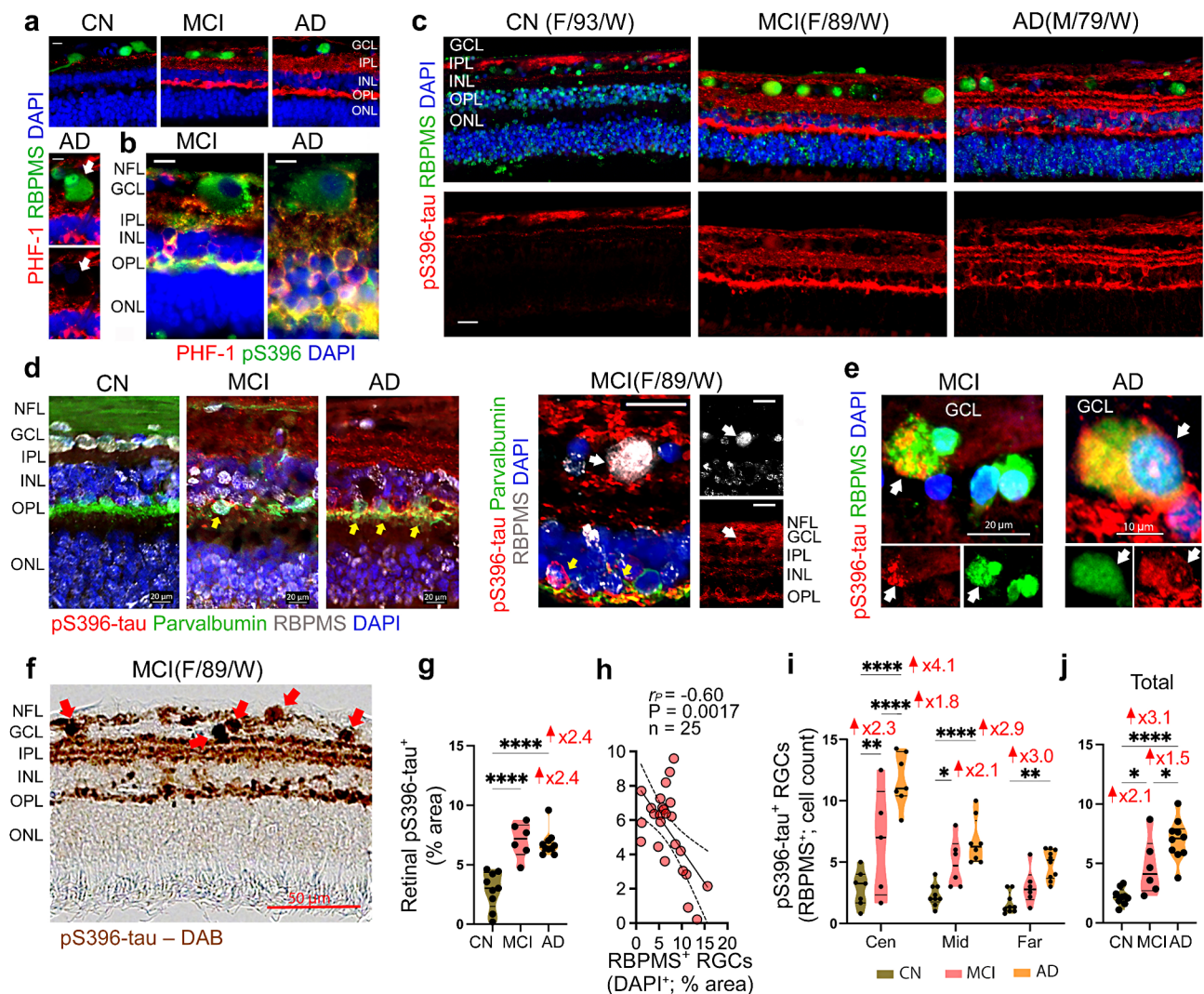


Fig. 3 Phosphorylated tau pathology in RGCs of MCI and AD patients. **(a)** Representative microscopic images of retinal cross-sections immunolabeled for paired helical filament of tau (PHF-1, red), RBPMS (green), and DAPI for nuclei (blue) in CN, MCI, and AD subjects. Scale bars: 10 μ m. PHF-tau is usually not found within RGCs of MCI and AD patients, as shown in top and bottom left panels and indicated by white arrows. **(b)** Representative microscopic images of retinal cross-sections immunofluorescently co-labeled for PHF-tau (PHF-1, red) and hyperphosphorylated (p)tau at S396 epitope (pS396-tau, green), with nuclei (DAPI, blue) in MCI and AD donors. Scale bars: 10 μ m. RGCs appear to stain for pS396-tau, and not PHF-tau, as shown by cell morphology and location in the GCL, while other layers (IPL, INL, OPL) show colocalization (yellow) of PHF-tau and pS396-tau. Scale bars: 10 μ m. **(c)** Representative micrographs of retinal cross-sections immunolabeled for pS396-tau (red), RGCs (RBPMS, green), and nuclei (DAPI, blue) in CN, MCI, and AD donors. Scale bars: 20 μ m. **(d)** Retinal micrographs immunolabeled for RBPMS RGCs (white), pS396-tau (red), amacrine and RGCs marker - parvalbumin (green), and nuclei (DAPI, blue) in CN, MCI, and AD subjects. Colocalization of pS396-tau in parvalbumin⁺ amacrine cells (yellow arrows, left panel) and RBPMS⁺ RGCs (white arrows, middle panel) are shown. Scale bars: 20 μ m. **(e)** High-magnification microscopic images depicting pS396-tau (red) accumulation in hypertrophic RBPMS⁺ RGCs (green); white arrows indicate pS396-tau-laden RGCs in MCI and AD patients (yellow for colocalization). Scale bars: 20 μ m (left) and 10 μ m (right). Bottom panels show separate channels for each pS396-tau and RBPMS. **(f)** A representative microscopic image of peroxidase-based staining for pS396-tau isoforms (brown) within retinal layers, and specifically, in RGCs (by morphology and location, red arrows) of an MCI patient. Scale bar: 50 μ m. **(g)** Quantification of pS396-tau percent area in the ST retina ($n=9$ CN, $n=6$ MCI, $n=10$ AD). **(h)** Pearson's correlation coefficient (r_p) analysis between retinal pS396-tau and RBPMS⁺ RGCs. **(i-j)** Cell count of pS396-tau⁺ RGCs in **(i)** Central, Mid-, and Far-peripheral retinal subregions, and **(j)** total ST retina ($n=19-25$). Individual data points and median, lower, and upper quartiles are shown in violin plots. * $P < 0.05$, ** $P < 0.01$, **** $P < 0.0001$, by one-way or two-way ANOVA followed by Tukey's post-hoc multiple comparison test. Fold changes are shown in red. F, female; M, male; Age (in years); Ethnicity: W, White; NFL, Nerve fiber layer, GCL, ganglion cell layer; IPL, Inner Plexiform Layer; INL, Inner Nuclear Layer, OPL, Outer Plexiform Layer; ONL, Outer Nuclear Layer; RGC, Retinal ganglion cells

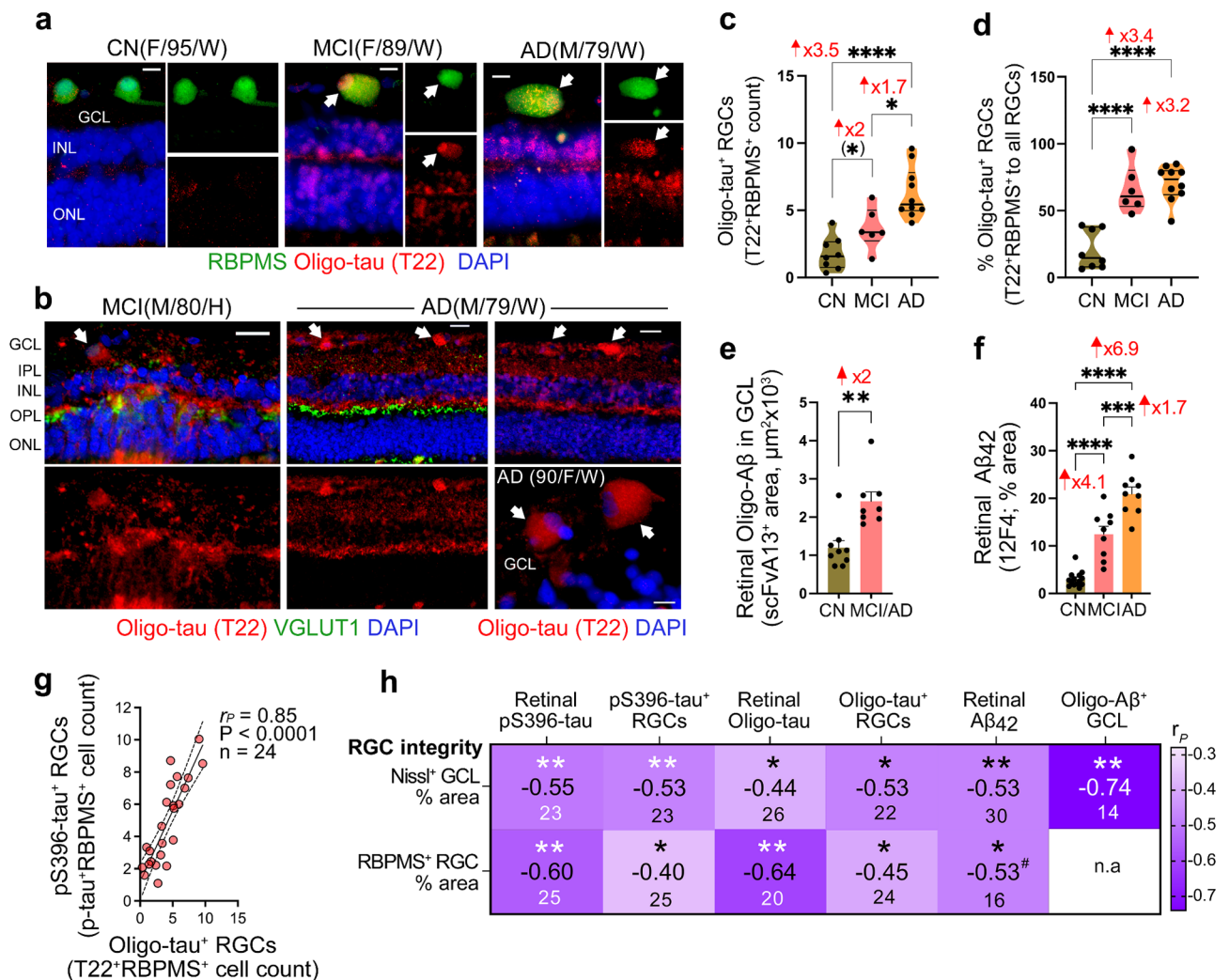


Fig. 4 Oligomeric tau isoforms within RGCs in MCI and AD patients. **(a)** Representative retinal cross-sections immunolabeled for Oligo-tau (T22, red), RBPMS⁺ RGCs (green), and nuclei (DAPI, blue), showing Oligo-tau colocalization in RGCs (yellow, white arrows) in MCI and AD vs. CN. Scale bars: 10 μm. **(b)** Representative retinal cross-sections immunolabeled for Oligo-tau (T22⁺, red), pre-synaptic marker VGLUT1 (green), and nuclei (DAPI, blue) in MCI and AD patients, showing Oligo-tau-laden RGCs, per morphology and cell layer (white arrows). Scale bars: 20 μm. **(c)** Quantification of T22⁺ Oligo-tau RBPMS⁺ RGC count in MCI ($n=6$) and AD ($n=10$) patients vs. CN controls ($n=8$). **(d)** Percent of Oligo-tau⁺ RBPMS⁺ RGC count to total RBPMS⁺ RGC count in this cohort. **(e)** Quantitative analysis of retinal Oligo-Aβ in the GCL (scFvA13⁺ immunoreactive area within β-III-tubulin⁺ neurons) in this cohort ($n=8$ MCI/AD, $n=9$ CN). **(f)** Quantitative analysis of retinal Aβ₄₂ percent area in this cohort ($n=9$ MCI, $n=9$ AD, $n=14$ CN). **(g)** Pearson's correlation coefficient (r_P) analysis between Oligo-tau⁺ RGC and pS396-tau⁺ RGC cell counts. **(h)** Heatmap displays Pearson's r_P correlations of RGC integrity parameters (% area of RBPMS⁺ RGCs and Nissl⁺ cells in GCL) with the following abnormal tau and Aβ forms in the retina and within RGCs: retinal pS396-tau (% area), pS396-tau⁺ RGCs (count), retinal T22⁺ Oligo-tau (% area), T22⁺ Oligo-tau⁺ RGCs (% cell count), retinal 12F4⁺ Aβ₄₂ (% area), and scFvA13⁺ Oligo-Aβ in the GCL (area). Large-font numbers indicate Pearson's r values and lower-font numbers indicate sample size (n). Individual data points and median, lower, and upper quartiles are shown in violin plots. Bar graphs display mean ± SEM. * $P < 0.05$, ** $P < 0.01$, *** $P < 0.001$, **** $P < 0.0001$, by one-way or two-way ANOVA followed by Tukey's post-hoc multiple comparison test or unpaired Student t -test (in parenthesis). Statistical significance shown in the heatmap is calculated by Pearson's correlation analyses. Fold changes are shown in red. F, female; M, male; Age (in years); Ethnicity: W, White and H, Hispanic; GCL, ganglion cell layer; IPL, Inner Plexiform Layer; INL, Inner Nuclear Layer, OPL, Outer Plexiform Layer; ONL, Outer Nuclear Layer; RGC, Retinal ganglion cells

Retinal pS396-tau and oligo-tau laden ganglion cells correlate with AD status

We further determined the potential relationship between pS396-tau⁺ or Oligo-tau⁺ RBPMS⁺ RGCs or RGC integrity, and the severity of AD-related brain pathology (Fig. 5a-k; extended data for correlations across retinal subregions in Table 2). Spearman's rank

correlation coefficient (r_S) analyses revealed that pS396-tau⁺ and Oligo-tau⁺ RGC counts moderate-to-strongly associated with brain Aβ-plaque burden (Fig. 5a, b; $r_S=0.52-0.63$, $P=0.013-0.0013$) and NFT severity scores (Fig. 5c, d; $r_S=0.70-0.72$, $P=0.0003-0.0001$). Stratifying patients based on Braak stage severity showed significant 1.9-2.7-fold increases in pS396-tau⁺ RBPMS⁺

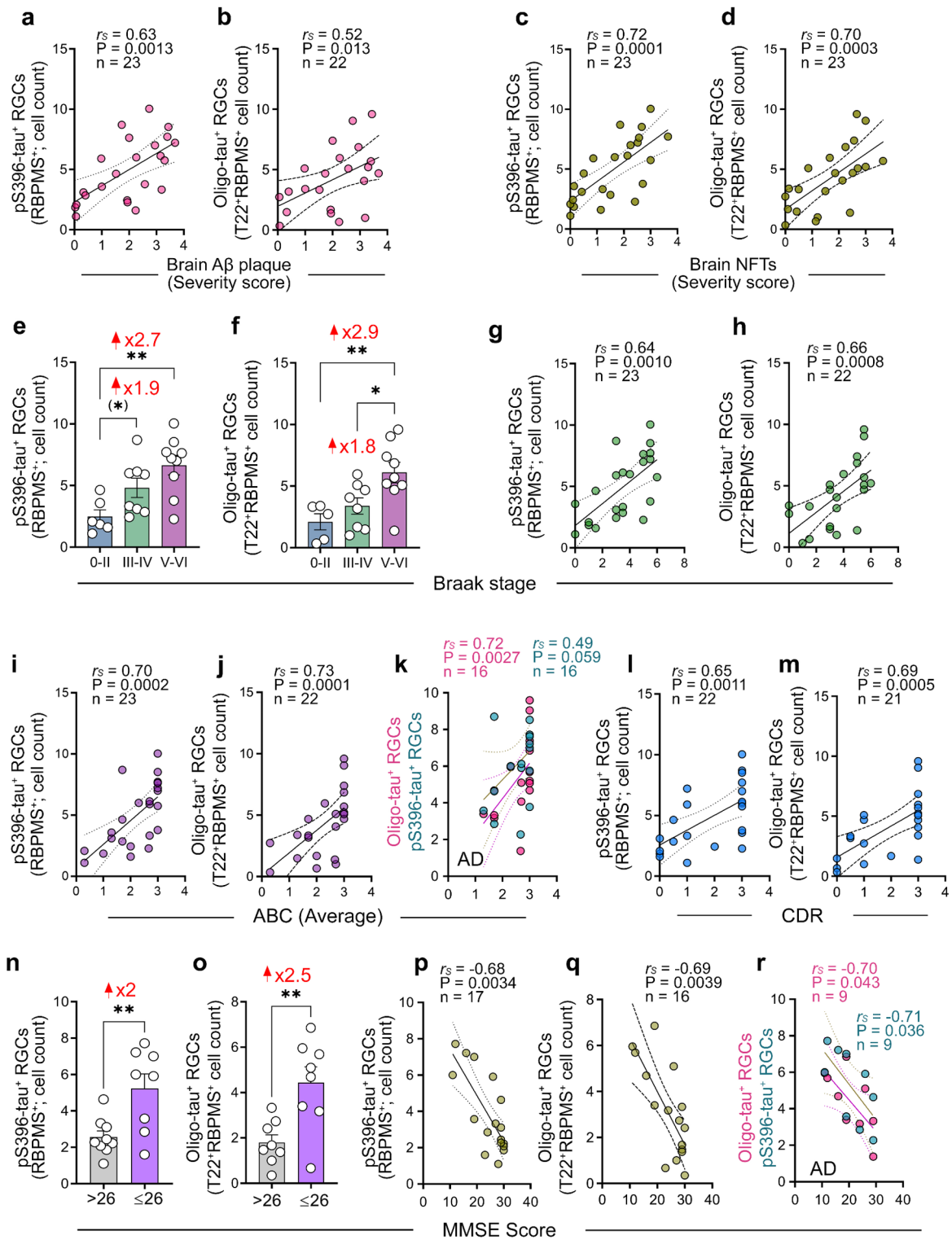


Fig. 5 (See legend on next page.)

(See figure on previous page.)

Fig. 5 Interactions of Oligo-tau and pS396-tau-laden RGCs with brain pathology and cognitive status. **(a-d)** Spearman's rank correlation coefficient (r_s) analyses of pS396-tau⁺ RGCs (count) or T22⁺ Oligo-tau⁺ RGCs (count) with **(a, b)** brain Aβ plaque severity scores or **(c, d)** brain neurofibrillary tangles (NFTs) severity scores. **(e, f)** Quantitative pS396-tau⁺ RGC and Oligo-tau⁺ RGC cell counts per Braak stage stratification ($n=22-23$). **(g, h)** Spearman's r_s correlations of **(g)** pS396-tau⁺ RGCs (count) or **(h)** Oligo-tau⁺ RGCs (count) with the Braak stage. **(i-m)** Spearman's r_s correlations of pS396-tau⁺ RGCs (count) or Oligo-tau⁺ RGCs (count) with **(i-k)** average brain ABC scores (**k** for MCI due-to-AD and AD dementia patients only), and with **(l-m)** clinical dementia rating (CDR) scores. **(n, o)** Quantitative pS396-tau⁺ RGC and Oligo-tau⁺ RGC cell counts when patients are stratified according to 26-score cutoff on the mini-mental state examination (MMSE; $n=16-17$). **(p-r)** Spearman's r_s correlations between pS396-tau⁺ RGCs or Oligo-tau⁺ RGCs cell counts and MMSE scores (**r** for MCI due-to-AD and AD dementia patients only). Bar graphs display individual data points and mean \pm SEM. * $P < 0.05$, ** $P < 0.01$, by one-way ANOVA followed by Tukey's post-hoc multiple comparison test. Two group comparison is determined by unpaired Student t -test. ABC scores comprise of mean grades for: **(A)** Aβ plaque score modified from Thal, **(B)** NFT stage modified from Braak, and **(C)** neuritic plaque score modified from CERAD

RGCs in the high (V-VI) and, to a lesser extent, the intermediate (III-IV) Braak stage groups compared to the low (0-II) group (Fig. 5e; $P < 0.05 - 0.01$). Similarly, Oligo-tau⁺ RBPMS⁺ RGCs were 2.9-fold elevated in the high (V-VI) Braak stage group compared to the low (0-II) group (Fig. 5f; $P < 0.05 - 0.01$). Both pS396-tau and Oligo-tau laden RGC counts were strongly correlated with Braak stage (Fig. 5g, h; $r = 0.64 - 0.66$, $P = 0.001 - 0.0008$). In addition, pS396-tau and Oligo-tau laden RGC counts were strongly correlated with ABC disease severity scores (Fig. 5i-k; $r = 0.70 - 0.73$, $P = 0.0002 - 0.0001$), with strong associations remaining when analyzed for MCI (due to AD) and AD patients only (Fig. 5k). No significant correlations were detected between RGC integrity parameters (RBPMS⁺ RGC count, Nissl⁺ in GCL % area) and any of the AD-related brain pathology scores

(Table 2). Interestingly, analyses per retinal subregions detected stronger associations to AD-brain pathology for *central* retinal pS396-tau⁺ RGCs and *mid-peripheral* Oligo-tau⁺ RGCs (Table 2), with a very strong association between mid-peripheral Oligo-tau⁺ RGCs and brain NFTs ($r_s = 0.81$, $P < 0.0001$).

Finally, we evaluated the associations between tau-laden RGC counts, RGC integrity parameters, and cognitive status, as measured by clinical dementia rating (CDR) and mini-mental state examination (MMSE) tests (Fig. 5l-r; extended data across retinal subregions in Table 3). No significant correlations were detected between RGC integrity parameters in the total ST retina and cognitive scores, whereas moderate-to-strong associations were observed in specific retinal subregions (Table 3). Strong correlations were found between both pS396-tau

Table 2 Correlations between RGC parameters and brain pathology

	Brain Aβ Plaque (score)		Brain NFTs (score)		BRAAK (stage)		ABC (score)	
	N = 17-23		N = 14-23		N = 17-23		N = 14-23	
	r_s	P	r_s	P	r_s	P	r_s	P
RBPMS⁺RGCs (count)								
Total	-0.17	0.44	-0.20	0.36	-0.16	0.46	-0.17	0.44
Central	-0.14	0.58	-0.17	0.50	-0.15	0.56	-0.17	0.51
Mid-periphery	-0.32	0.16	-0.33	0.14	-0.35	0.12	-0.40	0.073
Far-periphery	-0.25	0.24	-0.30	0.17	-0.28	0.20	-0.24	0.27
Nissl⁺in GCL (% area)								
Total	-0.14	0.56	-0.10	0.66	-0.019	0.93	-0.085	0.71
Central	-0.074	0.78	-0.23	0.38	-0.20	0.43	-0.17	0.50
Mid-periphery	-0.13	0.56	-0.092	0.69	-0.054	0.82	-0.11	0.63
Far-periphery	-0.35	0.13	-0.025	0.92	0.0084	0.97	-0.17	0.48
pS396-tau⁺RGCs (count)								
Total	0.63	0.0013**	0.72	0.0001***	0.64	0.0010**	0.70	0.0002***
Central	0.65	0.0034**	0.69	0.0014**	0.68	0.0020**	0.72	0.0008***
Mid-periphery	0.51	0.019*	0.74	0.0001***	0.64	0.0018**	0.61	0.0032**
Far-periphery	0.58	0.0039**	0.72	0.0001***	0.63	0.0012**	0.68	0.0003***
Oligo-tau⁺RGCs (count)								
Total	0.52	0.013*	0.70	0.0003***	0.66	0.0008***	0.73	0.0001***
Central	0.40	0.14	0.67	0.0073**	0.58	0.026*	0.59	0.022*
Mid-periphery	0.65	0.0035**	0.81	<0.0001****	0.78	0.0001***	0.79	<0.0001****
Far-periphery	0.26	0.24	0.50	0.017*	0.47	0.027*	0.47	0.029*

Spearman's rank correlation analyses: P and r_s -values determine the statistical significance and strength of each pairwise association between retinal RGC marker and brain pathology. P and r_s -values presented in bold type with asterisk(s) are statistically significant (< 0.05). Aβ, amyloid beta-protein; NFTs, neurofibrillary tangles. ABC scores comprise of mean grades for: (A) Aβ plaque score modified from Thal, (B) NFT stage modified from Braak, and (C) neuritic plaque score modified from CERAD

Table 3 Correlations between RGC parameters and the cognitive status

	CDR (score)		MMSE (score)	
	N=13–22		N=10–18	
	r_s	P	r_s	P
RBPMS⁺RGCs (count)				
Total	-0.33	0.13	0.26	0.31
Central	-0.06	0.83	0.15	0.59
Mid-periphery	-0.43	0.056	0.46	0.065
Far-periphery	-0.51	0.016*	0.32	0.20
Nissl⁺in GCL (% area)				
Total	-0.40	0.080	0.48	0.070
Central	-0.52	0.041*	0.28	0.35
Mid-periphery	-0.35	0.13	0.58*	0.024*
Far-periphery	-0.34	0.16	0.64*	0.012*
pS396-tau⁺RGCs (count)				
Total	0.65	0.0011**	-0.68	0.0034**
Central	0.61	0.011*	-0.62	0.015*
Mid-periphery	0.63	0.0030**	-0.58	0.017*
Far-periphery	0.65	0.0011**	-0.54	0.026*
Oligo-tau⁺RGCs (count)				
Total	0.69	0.0005***	-0.69	0.0039**
Central	0.68	0.0096**	-0.67	0.028*
Mid-periphery	0.64	0.0042**	-0.79	0.0019**
Far-periphery	0.39	0.0837	-0.41	0.1180

Spearman's rank correlation analyses: P and r_s -values determine the statistical significance and strength of each pairwise association between retinal RGC marker and the cognitive function score. P and r_s -values presented in bold type with asterisk(s) are statistically significant (<0.05). CDR, Clinical Dementia Rating; MMSE, Mini-Mental State Examination

and Oligo-tau laden RBPMS⁺ RGCs and CDR scores (Fig. 5l, m; $r=0.65-0.69$, $P=0.0011-0.0005$), for the total ST retina and most subregions (Table 3). Stratifying patients based on a MMSE cut-off score of 26, which has been reported to have high sensitivity and specificity for detecting dementia [90], was utilized in our cohort. This analysis showed a significant 2-2.5-fold increase in pS396-tau⁺ and Oligo-tau⁺ RGCs in the MMSE \leq 26 group compared to the MMSE $>$ 26 group (Fig. 5n, o; $P<0.01$). Strong inverse correlations were observed between pS396-tau⁺ or Oligo-tau⁺ RGCs and MMSE scores (Fig. 5p-r; $r=-0.68-(-0.69)$, $P=0.0039-0.0034$), including analyses restricted to MCI (due to AD) and AD patients (Fig. 5r), for both the total retina and across retinal subregions (Table 3; extended correlations for MCI and AD patients only in Suppl. Table 3).

Discussion

In this study, we present the first evidence of pathogenic tau inclusions, specifically pS396-tau and Oligo-tau, within RBPMS-positive RGCs, concomitant with ganglion cell loss (~50%) in the retinas of donor patients with MCI (due to AD) and AD dementia. Increases in these pretangle isoform-containing RGCs in both MCI and AD patients were accompanied by hypertrophic RGC

soma and nuclei displacement, as well as elevated apoptotic cell markers (~30%) and the expression of GVD (CHPM2B) and GVD-associated necroptotic (pMLKL) markers in RGCs. We revealed a very strong association between the two pretangle tau forms in RGCs. Notably, we found moderate to strong associations between RGC loss and retinal pS396-tau or Oligo-tau burden, including tau-laden RGCs. Retinal A β_{42} and intra-RGC A β oligomers also associated with RGC reduction, suggesting a link between retinal tau and amyloid pathologies and ganglion cell integrity in AD. Importantly, our data indicated tight correlations between pS396-tau or Oligo-tau-containing RGCs and respective brain pathology, disease stage, and cognitive status. The most consistent and strong correlations with brain pathology and cognition were found for pS396-tau-laden RGCs in the central/mid-peripheral subregions, and for Oligo-tau-laden RGCs in the mid-periphery. Overall, our findings suggest that abnormal tau isoforms accumulate within RBPMS⁺ RGCs in patients with MCI and AD, potentially contributing to early and pronounced RGC loss and showing a strong correlation with disease severity.

Among the RGC populations, midget cells projecting to the parvocellular (P-cell) layers of the lateral geniculate nucleus (LGN) and parasol cells projecting to the magnocellular (M-cell) layers of the LGN serve as two distinct visual pathways that process color and low spatial frequency contrast vision, respectively [72]. In AD patients, abnormalities in color vision, eye movement, contrast sensitivity, and visual integration have been detected early in disease progression [33, 38, 47, 75, 81, 105]. Therefore, fluctuations in color perception and abnormal contrast sensitivity in AD patients may be attributed to damage and loss of these RGC types, in addition to the involvement of horizontal and amacrine neurons. Here, the analysis of the RBPMS marker, a conserved RNA binding protein with a single RNA recognition motif expressed in RGCs of humans and animal models [87, 94], facilitates differentiation from other retinal cells [66, 95, 102], further validating our findings in RGCs. Our current analysis of RGC integrity in the superior temporal retina indicates marked decreases in RBPMS⁺ RGC counts or immunoreactive area (by 47–55% in MCI and 46–50% in AD) compared to CN controls, with similar degrees of decreases observed in GCL Nissl⁺ neurons (by 56% in MCI and 55% in AD patients). These results are consistent with previous studies reporting significant reductions in RGCs and GCL thickness in AD patients compared to control subjects [8, 16–18, 109].

Specifically, the RBPMS⁺ RGC count per retinal subregion indicated a 46% loss in MCI and a 57% loss in AD in the mid-periphery, as well as a 62% loss in MCI and a 45% loss in AD in the far periphery. Similarly, a study by Blanks et al., described GCL neuronal loss in AD as

most pronounced in the superior and inferior quadrants, ranging from 40 to 49% throughout the mid-peripheral subregions, and reaching 50–59% in the far-peripheral retina of AD patients [16]. These peripheral retinal subregions, which have anatomically fewer ganglion cells and a thinner nerve fiber layer, appear more vulnerable to RGC loss in AD, potentially due to a higher density of abnormal A β and tau species (e.g., A β ₄₂, A β oligomers, PHF-tau, pS396-tau, and pS202/T205-tau), and microgliosis [63, 64, 73, 112]. Interestingly, whereas the total and mid-peripheral ST retina consistently demonstrated significant and similar RGC reductions in both MCI and AD patients, as shown by the GCL Nissl⁺ area and RBPMS⁺ RGC count analyses, non-significant trends were noted for the far and central subregions, respectively. These differences may be due to variations in the types of analysis and staining patterns.

Importantly, the loss of RGCs in MCI and AD patients may explain previous reports of visual dysfunctions in AD, specifically impaired color vision, low spatial frequency contrast, and motion perception [38], which can be attributed, at least in part, to the loss of M-cell and P-cell RGCs. However, the retinal regions examined here align with the superior-temporal arcade along the temporal vessels, primarily containing axons from magnocellular pathway RGCs rather than those originating from macular areas. Consequently, the substantial RGC loss observed in these regions is unlikely to significantly affect fine or central vision provided by the macula. Having said that, Frisen and Quigley [36], in a landmark article, showed that even a 50% loss of optic nerve axons did not usually cause a diminution of visual acuity. Their histopathological study concluded that there are “extra axons” that represent redundancy. This is in close alignment with a study by Tenhula et al. [120], demonstrating histopathological counts versus loss of vision. More accurately, the “extra axons” lost probably provide for better contrast sensitivity and, indeed, AD patients suffer losses of contrast sensitivity [4, 38, 101, 104]. Subjectively, RGC losses of this magnitude are perhaps not sufficient to be described in routine neurological or ophthalmological examinations. Furthermore, many of the lost axons originate from magnocellular RGCs, which mediate low spatial frequency contrast sensitivity and motion perception. These deficits, though not consciously apparent to patients, can be objectively demonstrated through proper testing. As it relates to another functional impairment, a previous study of postmortem AD retinas identified a reduction in melanopsin retinal ganglion cells (mRGCs), intrinsically photosensitive cells that contribute to the photoentrainment of circadian rhythms, potentially explaining the sleep disturbances observed in these patients [70].

In the brains of AD patients, the increase in hyperphosphorylated tau isoforms has been shown to lead to tau aggregation, oligomerization, propagation, and NFT formation, ultimately causing neuronal dysfunction and degeneration [93, 119]. Previous studies have detected intracellular pretangles and mature tangles in the retinas of AD patients [28, 30, 40, 45, 46, 63, 89, 112, 129]. Recently, we also identified tau oligomers and citrullinated-tau, along with other tau isoforms, in the retinas of MCI and AD patients. Notably, both pS396-tau and oligomeric-tau forms were frequently observed within the GCL, with significant increases in MCI and AD patients [112]. The pS396-tau and Oligo-tau isoforms are increased in the AD brains and are linked to neuronal cell loss and Braak stage severity [9, 25, 39, 96, 104, 117, 133]. Here, we found a specific buildup of these pathological tau isoforms within RGCs of MCI and AD patients, demonstrating their very strong inter-relations and connection with RGC integrity, and entailing similar links between tauopathy and neurodegeneration in the retina, as observed in the brain.

In this study, we detected higher numbers of RBPMS⁺ RGCs containing pS396-tau and Oligo-tau in patients with AD dementia and those at the earliest stages of functional impairment (MCI due to AD). These pathogenic tau-laden RGC counts were higher in AD patients compared to MCI patients, suggesting that more RGCs are affected by pS396-tau and Oligo-tau as the disease progresses. Our data on pS396-tau and Oligo-tau laden RGCs across retinal subregions indicated that the most significant and substantial changes were detected in the central and mid-peripheral ST retina, with less pronounced changes in the far periphery. This could be attributed to the density of RGCs in each subregion, as there are up to eight layers of ganglion cells in the central subregion and only one or two layers, with space between them, in the far periphery [56]. Hence, there is a higher probability that RGCs in the central/middle subregions are impacted by pS396-tau and Oligo-tau compared to those in the far-peripheral retina. These findings may guide potential future in vivo imaging of tau-positive RGCs in the central and mid-peripheral ST retina for the early detection of AD.

In both fluorescent and peroxidase-based staining methods, we observed a three-parallel-string staining pattern of retinal pS396-tau in the IPL of MCI and AD patients. Consistent with retinal neuroanatomy, these findings suggest that pS396-tau accumulates within the neuronal dendrites of RGCs, which connect with the axons of bipolar and amacrine cells. These tau aggregates in synaptic-rich regions may interfere with information transmission and could help explain the decrease in contrast sensitivity observed in MCI and AD patients. Moreover, in MCI and AD patients, both pS396-tau and

Oligo-tau isoforms were observed in the OPL, the former was specifically found in parvalbumin⁺ horizontal cells. A recent study suggested that pS202/T205-tau (AT8⁺) spreads from the OPL to the IPL/GCL in the AD retina [129]. The patterns of retinal pS396-tau and Oligo-tau accumulation in CN subjects and MCI/AD patients (predominately in the IPL/OPL), merit further investigation to understand how pathogenic tau spreads across retinal layers and neuronal processes during AD progression.

Beyond the moderate-to-strong inverse correlations between RGC integrity and pS396-tau⁺ or Oligo-tau⁺ RGC counts, as well as retinal pS396-tau or Oligo-tau loads, our analysis showed a strong negative association between RGC reduction and intra-RGC A β oligomers, suggesting their substantial and detrimental effects on RGC degeneration. These retinal findings in AD are consistent with similar reports connecting elevated A β and tau oligomers with neuronal loss in AD brains [3, 9, 71, 86, 109, 123]. Notably, the levels of retinal A β ₄₂ also correlated with the extent of pS396-tau or Oligo-tau-laden RGCs (not shown; $r_p=0.69$ and $r_p=0.67$, respectively; $P=0.003$), as well as RGC integrity, suggesting that retinal A β may drive RGC tauopathy and degeneration, similar to the interactions between A β and the spread of tau in neurons of AD brains [18, 134].

Levels of the early apoptotic marker, cleaved caspase 3 [124], have been shown to be elevated in AD brains, with a high degree of colocalization to neurofibrillary tangles within neurons [39, 116]. In the current study, we observed increased CCasp3 expression in GCL cells, specifically in ~30% of RBPMS⁺ RGCs in AD dementia patients, but not in MCI patients compared to cognitively normal controls. This is consistent with previous studies showing increased CCasp3⁺/Tuj1⁺ RGCs [40] and overall retinal CCasp3 expression [64] in AD patients compared to controls. The elevated expression of retinal CCasp3 in RGCs, along with significant interactions with pS396-tau and Oligo-tau-laden RGCs, suggests that these pathogenic tau forms may trigger apoptotic RGC death in a later disease stage.

RGCs are highly diverse, consisting of multiple subtypes that exhibit a range of morphological and physiological characteristics, including variations in soma and cell body size [56]. In this study, we observed that RGCs in aged CN individuals predominantly had small-sized somas, with a minority of cells exhibiting large, round somas. In contrast, a higher number of RGCs in MCI and AD patients appeared swollen, with enlarged somas and displaced nuclei, particularly in those containing pS396-tau or Oligo-tau inclusions. Notably, RBPMS⁺ RGCs in these patients exhibited granulovacuolar degeneration (GVD) bodies marked by CHMP2B [130] and expressed the GVD-necroptotic marker pMLKL [61], suggesting that RGCs in early and advanced AD patients undergo

cell death via GVD-mediated necroptosis. To the best of our knowledge, this is the first demonstration of hypertrophic RGCs expressing GVD bodies and GVD-necroptotic markers in MCI and AD patients. This abnormal RGC phenotype is characteristic of neurons exhibiting GVD-associated activation of the necroptosis pathway, indicated by phosphorylated MLKL-positive GVD bodies [60, 130]. This process has been observed in the brains of individuals with preclinical AD and AD dementia [62, 64, 121]. The morphology and process of necroptotic cells are characterized by compromised plasma membrane integrity, organelle and cell enlargement, chromatin fragmentation, and eventual cell lysis [92, 133]. Moreover, studies have indicated that necroptosis is involved in AD brain pathology and is closely linked to tau pathology and Braak stage progression [11, 21, 49, 64], with recent research showing that p-tau contributes to neuronal death by inducing necroptosis and inflammation [29]. In this study, the abnormal phenotype of RGCs, particularly in those with pS396-tau or Oligo-tau accumulation, may indicate necroptotic cell death in the RGCs of AD retinas. Future studies are needed to determine the predominant mechanism of retinal ganglion cell death and the role of pathogenic tau in apoptotic and necroptotic RGC loss in AD.

Our analysis of the potential connections between pS396-tau or Oligo-tau-containing RGCs and disease status indicates strong associations between both pretangle tau forms in RGCs and the following brain pathologies: A β plaques, NFTs, Braak stage, and ABC neuropathic changes. However, RGC counts alone did not correlate with these AD brain parameters. These data suggest that tauopathy-laden RGCs may represent the link between retinal neuronal injury and brain AD pathology and disease progression. Importantly, our data indicate that pS396-tau and Oligo-tau-containing RGC counts strongly correlate with cognitive status, as measured by the CDR and MMSE scores. While the CDR is a test that assess cognitive, behavioral, and functional performance associated with AD, the MMSE test evaluates cerebral competency, comprehension, and communication. We believe the strong correlations between pS396-tau⁺ or Oligo-tau⁺ RBPMS⁺ RGCs and disease parameters primarily reflect the accumulation of these tauopathy forms in the retina of AD patients. While RGC loss may have contributed modestly to these correlations, it does not independently predict tau or A β pathology in the brain, nor their Braak staging or ABC scoring. While cell loss is a significant feature of AD, it often does not directly correlate with the severity of brain A β and tau pathology. However, the observed correlations between RGC loss (in specific retinal subregions) and cognitive score (CDR, MMSE), suggest a potential link between retinal ganglion cell death and cognitive function in AD, as in the brain.

These findings highlight that a future retinal imaging approach, which reliably measures RGC-containing tauopathy in ST central or mid-peripheral subregions holds potential as a more robust biomarker, compared to RGC integrity or retinal tauopathy alone, for imaging AD progression and monitoring disease status, in both early and advanced AD. In the clinical setting, the GCL layer is assessed by OCT [38, 76, 78, 113], and apoptotic RGCs can be imaged using the detection of apoptotic retinal cells (DARC) method [10, 27]. More specific RGC changes could be detectable in the inner retina using high-resolution imaging systems, such as AO-OCT. Imaging RGCs, combined with future tauopathy tracers, could serve as a non-invasive biomarker for early AD diagnosis and monitoring of disease progression. This approach would be immensely valuable in future trials evaluating new treatments for AD.

We acknowledge several limitations of this study. As a cross-sectional, case-control study, our focus was primarily on group stratification and correlations, so caution must be exercised before implicating cause-and-effect conclusions. Moreover, the lack of clinical information on visual system-related symptoms limits our ability to assess potential connections between pS396-tau⁺ or Oligo-tau⁺ RBPMS⁺ RGCs and various manifestations of visual dysfunction. This highlights the need for future studies to explore the relationships between tauopathy-laden RGCs, RGC loss, and ocular outcomes in patients. Additionally, larger and more diverse populations are needed to validate these findings and to compare RGC susceptibility with that of other retinal cell types in relation to AD processes.

Conclusion

In summary, this study provides the first evidence of RGCs laden with abnormal tau inclusions, including pS396-tau and oligomeric tau, in early (MCI) and AD dementia patients, with clear indications of increased RGC vulnerability. RBPMS-positive RGCs containing pS396-tau or Oligo-tau were increased in MCI and AD patients, and these cells exhibited hypertrophic cell somas as well as apoptotic and GVD/GVD-necroptotic markers. These findings correlated with reduced RGC counts, suggesting that these tau pathologies may contribute to ganglion cell death in AD. Notably, strong correlations were found between pS396-tau and Oligo-tau laden RGCs and brain AD pathology, disease stage, and cognitive status. This study highlights the potential of imaging tau-laden RGCs as a non-invasive biomarker for early AD diagnosis and monitoring disease progression. However, further research is needed to more definitively establish these connections.

Abbreviations

A	Amyloid
Ab	Antibody
ABC	Amyloid/Braak/CERAD score
AD	Alzheimer's disease
ADRC	Alzheimer's disease research center
A β	Amyloid β -protein
ANOVA	Analysis of variance
B	Brain
Cen (C)	Central retina
CHMP2B	charged multivesicular body protein 2B
CCasp3	Cleaved caspase 3
CDR	Clinical Dementia Rating
CN	Cognitively normal
DAB	3,3'-Diaminobenzidine
F	Female
Far (F)	Far-peripheral retina
scFvA13	Single-chain Fv fragment A13 recognizing intraneuronal A β oligomers
GCL	Ganglion cell layer
GVD	granulovacuolar degeneration
H	Hispanic
IHC	Immunohistochemistry
INL	Inner nuclear layer
IPL	Inner plexiform layer
IR area	Immunoreactive area
M	Male
mAb	Monoclonal antibody
Mid (M)	Middle-peripheral retina
MCI	Mild Cognitive Impairment
MMSE	Mini-mental state examination
mRGC	Melanopsin Retinal Ganglion Cell
NDRI	National disease research interchange
NFL	Nerve fiber layer
NFT	Neurofibrillary tangle
NT	Neuropil thread
OD	Optic disc
Oligo	A β -Oligomeric amyloid β -protein
Oligo	tau-Oligomeric tau
ONL	Outer nuclear layer
OPL	Outer plexiform layer
pAb	Polyclonal antibody
PHF	Paired Helical Filaments
Phospho	MLKL-Phosphorylated Mixed Lineage Kinase Domain-Like
PMI	Postmortem interval
p	tau-Hyperphosphorylated tau
RBPMS	Ribonucleic acid binding protein with multiple splicing
RGC	Retinal Ganglion Cell(s)
Serine 396	S396
SD	Standard deviation
SEM	Standard error of the mean
ST	Superior temporal
VGLUT	1-Vesicular glutamate transporter 1
W	White

Supplementary Information

The online version contains supplementary material available at <https://doi.org/10.1186/s40478-025-01935-y>.

Supplementary Material 1

Acknowledgements

We thank Elijah Maxfield for assisting with manuscript editing. We thank Prof. Carol Ann Miller, the former director of the USC-ADRC neuropathology core laboratory, for providing the neuropathological reports. We thank the late Prof. Peter Davies of The Litwin-Zucker Research Center for the Study of Alzheimer's Disease, The Feinstein Institutes for Medical Research, New York, for providing

the PHF-1 antibodies. We thank Drs. Giovanni Meli and Antonino Cattaneo for the antibodies against A β oligomers (scFvA13). The authors dedicate this manuscript to the memory of Dr. Salomon Moni Hamaoui and Lillian Jones Black, both of whom died from Alzheimer's disease.

Author contributions

M.R.D.: performed experiments, collected, and analyzed data, created figures, drafted, and edited the manuscript. E.R., A.R., B.P.G., E.S.-G.: performed experiments, collected, and analyzed data. D.-T.F.: analyzed data, created figures and illustrations, edited and revised the manuscript. Y.K.: performed experiments, analyzed data, created figures, wrote, edited, and revised the manuscript. N.M.: assisted with experimental design and execution, collected data. L.S., D.H. provided donor eyes and the clinical and brain pathological data. R.K.: generated and provided the T22 antibodies that recognize tau oligomers. A.A.S., A.V.L., K.L.B.: assisted with interpretation of data and editing. M.K.-H. was responsible for study conception and design, data analysis and collection, interpretation of data, figure creation, study supervision, and manuscript writing, editing and revision. All authors have read and approved the manuscript.

Funding

This work has been supported by the National Institutes of Health (NIH)/the National Institute on Aging (NIA) through the following grants: R01 AG055865 and R01 AG056478 (M.K.H.), The Hertz Innovation Fund (M.K.H.), and the Gordon, Goldrich, Wilstein, and Saban Private Foundations (M.K.H.). Y.K., A.R., B.P.G., D.-T.F., M.K.H. are also supported, in part, by the NIH/NIA R01AG075998 grant. M.R.D. and E.R. are supported by The Ray Charles Foundation. E.S.G. is supported by José Castillejo grants for mobility stays abroad for young doctors 2023 (CAS22/00049, Ministerio de Ciencia, Investigación y Universidades) and Complutense del Amo Grants 2023, Complutense University of Madrid.

Data availability

The raw datasets analyzed during the current study are available from the corresponding author on reasonable request.

Declarations

Ethics approval and consent to participate

This study is not considered a human subjects research, and we confirm that consent was not necessary, for the reasons described as follow: we processed and analyzed deidentified retinal tissues of deceased patients that were provided by the USC-ADRC (IRB protocol HS-042071) and NDRI (Cedars-Sinai Medical Center IRB protocol Pro00019393). Histological studies at Cedars-Sinai Medical Center were performed under IRB protocols Pro00053412 and Pro00019393.

Consent for publication

Not applicable.

Competing interests

The authors declare no competing interests specific to this research work.

Author details

¹Department of Neurosurgery, Maxine Dunitz Neurosurgical Research Institute, Cedars-Sinai Medical Center, 127 S. San Vicente Blvd., A6212, Los Angeles, CA 90048, USA

²Institute of Ophthalmologic Research Ramón Castroviejo, Complutense University of Madrid, Madrid 28040, Spain

³Department of Immunology, Ophthalmology and ENT, Faculty of Optics and Optometry, Complutense University of Madrid, Madrid 28040, Spain

⁴Health Research Institute, Clinico San Carlos Hospital (IdISSC), Madrid 28040, Spain

⁵Mitchell Center for Neurodegenerative Diseases, University of Texas Medical Branch, Galveston, TX, USA

⁶Departments of Neurology, Neuroscience, and Cell Biology, University of Texas Medical Branch, Galveston, TX, USA

⁷Department of Ophthalmology, David Geffen School of Medicine, University of California Los Angeles, Los Angeles, CA, USA

⁸Doheny Eye Institute, Los Angeles, CA, USA

⁹Eye Program, Board of Governors Regenerative Medicine Institute, Cedars-Sinai Medical Center, Los Angeles, CA, USA

¹⁰Department of Biomedical Sciences, Division of Applied Cell Biology and Physiology, Cedars-Sinai Medical Center, Los Angeles, CA, USA

¹¹Alzheimer's Disease Research Center, Keck School of Medicine, University of Southern California, Los Angeles, CA, USA

¹²Department of Neurology, Cedars-Sinai Medical Center, Los Angeles, CA, USA

Received: 14 September 2024 / Accepted: 25 January 2025

Published online: 15 February 2025

References

- (2024) 2024 Alzheimer's disease facts and figures. *Alzheimers Dement* 20: 3708–3821 <https://doi.org/10.1002/alz.13809>
- Alexandrov PN, Pogue A, Bhattacharjee S, Lukiw WJ (2011) Retinal amyloid peptides and complement factor H in transgenic models of Alzheimer's disease. *NeuroReport* 22(12):623–627. <https://doi.org/10.1097/WNR.0b013e3283497334>
- Arendt T, Bruckner MK, Morawski M, Jager C, Gertz HJ (2015) Early neurone loss in Alzheimer's disease: cortical or subcortical? *Acta Neuropathol Commun* 3:10. <https://doi.org/10.1186/s40478-015-0187-1>
- Armstrong R, Kergoat H (2015) Oculo-visual changes and clinical considerations affecting older patients with dementia. *Ophthalmic Physiol Opt* 35(4):352–376. <https://doi.org/10.1111/opo.12220>
- Asanad S, Fantini M, Sultan W, Nassisi M, Felix CM, Wu J, Karanjia R, Ross-Cisneros FN, Sagare AP, Zlokovic BV et al (2020) Retinal nerve fiber layer thickness predicts CSF amyloid/tau before cognitive decline. *PLoS ONE* 15:e0232785. <https://doi.org/10.1371/journal.pone.0232785>
- Asanad S, Felix CM, Fantini M, Harrington MG, Sadun AA, Karanjia R (2021) Retinal ganglion cell dysfunction in preclinical Alzheimer's disease: an electrophysiologic biomarker signature. *Sci Rep* 11:6344. <https://doi.org/10.1038/s41598-021-85010-1>
- Asanad S, Ross-Cisneros FN, Nassisi M, Barron E, Karanjia R, Sadun AA (2019) The retina in Alzheimer's Disease: histomorphometric analysis of an ophthalmologic biomarker. *Invest Ophthalmol Vis Sci* 60:1491–1500. <https://doi.org/10.1167/iov.18-25966>
- Ashraf G, McGuinness M, Khan MA, Obtinalla C, Hadoux X, van Wijngaarden P (2023) Retinal imaging biomarkers of Alzheimer's disease: a systematic review and meta-analysis of studies using brain amyloid beta status for case definition. *Alzheimers Dement (Amst)* 15(2):e12421. <https://doi.org/10.1002/dad2.12421>
- Baker-Nigh A, Vahedi S, Davis EG, Weintraub S, Bigio EH, Klein WL, Geula C (2015) Neuronal amyloid-beta accumulation within cholinergic basal forebrain in ageing and Alzheimer's disease. *Brain* 138(6):1722–1737. <https://doi.org/10.1093/brain/awv024>
- Balendra SI, Normando EM, Bloom PA, Cordeiro MF (2015) Advances in retinal ganglion cell imaging. *Eye (Lond)* 29:1260–1269. <https://doi.org/10.1038/eye.2015.154>
- Balusu S, De Strooper B (2024) The necroptosis cell death pathway drives neurodegeneration in Alzheimer's disease. *Acta Neuropathol* 147:96. <https://doi.org/10.1007/s00401-024-02747-5>
- Besser L, Kukull W, Knopman DS, Chui H, Galasko D, Weintraub S, Jicha G, Carlsson C, Burns J, Quinn J et al (2018) Version 3 of the national alzheimer's coordinating center's uniform data set. *Alzheimer Dis Assoc Disord* 32(4):351–358. <https://doi.org/10.1097/WAD.0000000000000279>
- Bevan RJ, Hughes TR, Williams PA, Good MA, Morgan BP, Morgan JE (2020) Retinal ganglion cell degeneration correlates with hippocampal spine loss in experimental Alzheimer's disease. *Acta Neuropathol Commun* 8(1):216. <https://doi.org/10.1186/s40478-020-01094-2>
- Blair LJ, Nordhues BA, Hill SE, Scaglione KM, O'Leary JC 3rd, Fontaine SN, Breydo L, Zhang B, Li P, Wang L et al (2013) Accelerated neurodegeneration through chaperone-mediated oligomerization of tau. *J Clin Invest* 123(10):4158–4169. <https://doi.org/10.1172/JCI69003>
- Blanks JC, Hinton DR, Sadun AA, Miller CA (1989) Retinal ganglion cell degeneration in Alzheimer's disease. *Brain Res* 501:364–372. [https://doi.org/10.1016/0006-8993\(89\)90653-7](https://doi.org/10.1016/0006-8993(89)90653-7)
- Blanks JC, Schmidt SY, Torigoe Y, Porrello KV, Hinton DR, Blanks RH (1996) Retinal pathology in Alzheimer's disease. II. Regional neuron loss and glial changes in GCL. *Neurobiol Aging* 17(3):385–395. [https://doi.org/10.1016/0197-4580\(96\)00009-7](https://doi.org/10.1016/0197-4580(96)00009-7)

17. Blanks JC, Torigoe Y, Hinton DR, Blanks RH (1996) Retinal pathology in Alzheimer's disease. I. Ganglion cell loss in foveal/parafoveal retina. *Neurobiol Aging* 17(3):377–384. [https://doi.org/10.1016/0197-4580\(96\)00010-3](https://doi.org/10.1016/0197-4580(96)00010-3)
18. Bloom GS (2014) Amyloid-beta and tau: the trigger and bullet in Alzheimer disease pathogenesis. *JAMA Neurol* 71(4):505–508. <https://doi.org/10.1001/jamaneurol.2013.5847>
19. Braak H, Alafuzoff I, Arzberger T, Kretschmar H, Del Tredici K (2006) Staging of Alzheimer disease-associated neurofibrillary pathology using paraffin sections and immunocytochemistry. *Acta Neuropathol* 112(4):389–404. <https://doi.org/10.1007/s00401-006-0127-z>
20. Brier MR, Gordon B, Friedrichsen K, McCarthy J, Stern A, Christensen J, Owen C, Aldea P, Su Y, Hassenstab J et al (2016) Tau and Abeta imaging, CSF measures, and cognition in Alzheimer's disease. *Sci Transl Med* 8:338ra66. <https://doi.org/10.1126/scitranslmed.aaf2362>
21. Caccamo A, Branca C, Piras IS, Ferreira E, Huentelman MJ, Liang WS, Readhead B, Dudley JT, Spangenberg EE, Green KN et al (2017) Necroptosis activation in Alzheimer's disease. *Nat Neurosci* 20(9):1236–1246. <https://doi.org/10.1038/nn.4608>
22. Cao KJ, Kim JH, Kroeger H, Gaffney PM, Lin JH, Sigurdson CJ, Yang J (2021) ARCAM-1 facilitates fluorescence detection of amyloid-containing deposits in the Retina. *Transl Vis Sci Technol* 10(7):5. <https://doi.org/10.1167/tvst.10.7.5>
23. Chen S, Zhang D, Zheng H, Cao T, Xia K, Su M, Meng Q (2023) The association between retina thinning and hippocampal atrophy in Alzheimer's disease and mild cognitive impairment: a meta-analysis and systematic review. *Front Aging Neurosci* 15:1232941. <https://doi.org/10.3389/fnagi.2023.1232941>
24. Chiassou M, Alarcon-Martinez L, Belforte N, Quintero H, Dotigny F, Destrois-maisons L, Vande Velde C, Panayi F, Louis C, Di Polo A (2017) Tau accumulation in the retina promotes early neuronal dysfunction and precedes brain pathology in a mouse model of Alzheimer's disease. *Mol Neurodegener* 12(1):58. <https://doi.org/10.1186/s13024-017-0199-3>
25. Colom-Cadena M, Davies C, Sirisi S, Lee JE, Simzer EM, Tzioras M, Querol-Vilaseca M, Sanchez-Aced E, Chang YY, Holt K et al (2023) Synaptic oligomeric tau in Alzheimer's disease - A potential culprit in the spread of tau pathology through the brain. *Neuron* 111(14):2170–2183.e6. <https://doi.org/10.1016/j.neuron.2023.04.020>
26. Coppola G, Di Renzo A, Ziccardi L, Martelli F, Fadda A, Manni G, Barboni P, Pierelli F, Sadun AA, Parisi V (2015) Optical coherence tomography in Alzheimer's Disease: a Meta-analysis. *PLoS ONE* 10(8):e0134750. <https://doi.org/10.1371/journal.pone.0134750>
27. Cordeiro MF, Hill D, Patel R, Corazza P, Maddison J, Younis S (2022) Detecting retinal cell stress and apoptosis with DARC: progression from lab to clinic. *Prog Retin Eye Res* 86:100976. <https://doi.org/10.1016/j.preteyeres.2021.100976>
28. den Haan J, Morrema THJ, Verbraak FD, de Boer JF, Scheltens P, Rozemuller AJ, Bergen AAB, Bouwman FH, Hoozemans JJ (2018) Amyloid-beta and phosphorylated tau in post-mortem Alzheimer's disease retinas. *Acta Neuropathol Commun* 6(1):147. <https://doi.org/10.1186/s40478-018-0650-x>
29. Dong Y, Yu H, Li X, Bian K, Zheng Y, Dai M, Feng X, Sun Y, He Y, Yu B et al (2022) Hyperphosphorylated tau mediates neuronal death by inducing necroptosis and inflammation in Alzheimer's disease. *J Neuroinflammation* 19:205. <https://doi.org/10.1186/s12974-022-02567-y>
30. Du X, Koronyo Y, Mirzaei N, Yang C, Fuchs DT, Black KL, Koronyo-Hamaoui M, Gao L (2022) Label-free hyperspectral imaging and deep-learning prediction of retinal amyloid beta-protein and phosphorylated tau. *PNAS Nexus* 1(4):pgac164. <https://doi.org/10.1093/pnasnexus/pgac164>
31. Dumitrascu OM, Lyden PD, Torbati T, Sheyn J, Sherzai A, Sherzai D, Sherman DS, Rosenberry R, Cheng S, Johnson KO et al (2020) Sectoral segmentation of retinal amyloid imaging in subjects with cognitive decline. *Alzheimers Dement (Amst)* 12(1):e12109. <https://doi.org/10.1002/dad2.12109>
32. Dumitrascu OM, Rosenberry R, Sherman DS, Khansari MM, Sheyn J, Torbati T, Sherzai A, Sherzai D, Johnson KO, Czeszynski AD et al (2021) Retinal Venular Tortuosity jointly with retinal amyloid Burden correlates with Verbal Memory loss: a pilot study. *Cells* 10(11):2926. <https://doi.org/10.3390/cells10112926>
33. Elvira-Hurtado L, Lopez-Cuenca I, de Hoz R, Salas M, Sanchez-Puebla L, Ramirez-Torano F, Matamoros JA, Fernandez-Albarral JA, Rojas P, Alfonso S (2023) Alzheimer's disease: a continuum with visual involvements. *Front Psychol* 14:1124830. <https://doi.org/10.3389/fpsyg.2023.1124830>
34. Erskine L, Herrera E (2014) Connecting the retina to the brain. *ASN Neuro* 6(6):1759091414562107. <https://doi.org/10.1177/1759091414562107>
35. Folstein MF, Folstein SE, McHugh PR (1975) Mini-mental state. A practical method for grading the cognitive state of patients for the clinician. *J Psychiatr Res* 12:189–198. [https://doi.org/10.1016/0022-3956\(75\)90026-6](https://doi.org/10.1016/0022-3956(75)90026-6)
36. Frisen L, Quigley HA (1984) Visual acuity in optic atrophy: a quantitative clinicopathological analysis. *Graefes Arch Clin Exp Ophthalmol* 222:71–74. <https://doi.org/10.1007/BF02150634>
37. Frontzkowski L, Ewers M, Brendel M, Biel D, Ossenkopp R, Hager P, Steward A, Dewenter A, Romer S, Rubinski A et al (2022) Earlier Alzheimer's disease onset is associated with tau pathology in brain hub regions and facilitated tau spreading. *Nat Commun* 13:4899. <https://doi.org/10.1038/s41467-022-32592-7>
38. Gaire BP, Koronyo Y, Fuchs D-T, Shi H, Rentsendorj A, Danziger R, Vit J-PS, Mirzaei N, Doustar J, Sheyn J et al (2024) Alzheimer's disease pathophysiology in the retina. *Prog Retin Eye Res* 101:101273. <https://doi.org/10.1016/j.preteyeres.2024.101273>
39. Gastard MC, Troncoso JC, Koliatsos VE (2003) Caspase activation in the limbic cortex of subjects with early Alzheimer's disease. *Ann Neurol* 54(3):393–398. <https://doi.org/10.1002/ana.10680>
40. Grimaldi A, Pediconi N, Oieni F, Pizzarelli R, Rosito M, Giubettini M, Santini T, Limatola C, Ruocco G, Ragozzino D et al (2019) Neuroinflammatory processes, A1 astrocyte activation and protein aggregation in the retina of Alzheimer's disease patients, possible biomarkers for early diagnosis. *Front Neurosci* 13:925. <https://doi.org/10.3389/fnins.2019.00925>
41. Groot C, Smith R, Stomrud E, Binette AP, Leuzy A, Wuestefeld A, Wisse LEM, Palmqvist S, Mattsson-Carlgen N, Janelidze S (2023) phospho-tau with subthreshold tau-PET predicts increased tau accumulation rates in amyloid-positive individuals. *Brain* 146(4):1580–1591. <https://doi.org/10.1093/brain/awac329>
42. Grundke-Iqbal I, Iqbal K, Tung YC, Quinlan M, Wisniewski HM, Binder LI (1986) Abnormal phosphorylation of the microtubule-associated protein tau (tau) in Alzheimer cytoskeletal pathology. *Proc Natl Acad Sci U S A* 83:4913–4917. <https://doi.org/10.1073/pnas.83.13.4913>
43. Hadoux X, Hui F, Lim JKH, Masters CL, Peabay A, Chevalier S, Ha J, Loi S, Fowler CJ, Rowe C et al (2019) Non-invasive in vivo hyperspectral imaging of the retina for potential biomarker use in Alzheimer's disease. *Nat Commun* 10:4227. <https://doi.org/10.1038/s41467-019-12242-1>
44. Hammer DX, Agrawal A, Villanueva R, Saedi O, Liu Z (2020) Label-free adaptive optics imaging of human retinal macrophage distribution and dynamics. *Proc Natl Acad Sci USA* 117(48):30661–30669. <https://doi.org/10.1073/pnas.2010943117>
45. Hart de Ruyter FJ, Evers M, Morrema THJ, Dijkstra AA, den Haan J, Twisk JWR, de Boer JF, Scheltens P, Bouwman FH, Verbraak FD et al (2024) Neuropathological hallmarks in the post-mortem retina of neurodegenerative diseases. *Acta Neuropathol* 148(1):24. <https://doi.org/10.1007/s00401-024-02769-z>
46. Hart de Ruyter FJ, Morrema THJ, den Haan J, Nethertheless Brain B, Twisk JWR, de Boer JF, Scheltens P, Boon BDC, Thal DR, Rozemuller AJ et al (2022) Phosphorylated tau in the retina correlates with tau pathology in the brain in Alzheimer's disease and primary tauopathies. *Acta Neuropathol* 145(2):197–218. <https://doi.org/10.1007/s00401-022-02525-1>
47. Hart NJ, Koronyo Y, Black KL, Koronyo-Hamaoui M (2016) Ocular indicators of Alzheimer's: exploring disease in the retina. *Acta Neuropathol* 132(6):767–787. <https://doi.org/10.1007/s00401-016-1613-6>
48. Hinton DR, Sadun AA, Blanks JC, Miller CA (1986) Optic-nerve degeneration in Alzheimer's disease. *N Engl J Med* 315:485–487. <https://doi.org/10.1056/NEJM198608213150804>
49. Hoozemans JJ, van Haastert ES, Nijholt DA, Rozemuller AJ, Eikelenboom P, Scheper W (2009) The unfolded protein response is activated in pretangle neurons in Alzheimer's disease hippocampus. *Am J Pathol* 174:1241–1251. <https://doi.org/10.2353/ajpath.2009.080814>
50. Hyman BT, Phelps CH, Beach TG, Bigio EH, Cairns NJ, Carrillo MC, Dickson DW, Duycckaerts C, Frosch MP, Masliah E et al (2012) National Institute on Aging-Alzheimer's Association guidelines for the neuropathologic assessment of Alzheimer's disease. *Alzheimers Dement* 8:1–13. <https://doi.org/10.1016/j.jalz.2011.10.007>
51. Iqbal K, Wisniewski HM, Shelanski ML, Brostoff S, Liwnicz BH, Terry RD (1974) Protein changes in senile dementia. *Brain Res* 77:337–343. [https://doi.org/10.1016/0006-8993\(74\)90798-7](https://doi.org/10.1016/0006-8993(74)90798-7)
52. Jack CR Jr, Bennett DA, Blennow K, Carrillo MC, Dunn B, Haeberlein SB, Holtzman DM, Jagust W, Jessen F, Karlawish J et al (2018) NIA-AA Research Framework: Toward a biological definition of Alzheimer's disease. *Alzheimers Dement* 14:535–562. <https://doi.org/10.1016/j.jalz.2018.02.018>
53. Kadar A, Wittmann G, Liposits Z, Fekete C (2009) Improved method for combination of immunocytochemistry and nissl staining. *J Neurosci Methods* 184:115–118. <https://doi.org/10.1016/j.jneumeth.2009.07.010>

54. Katz B, Rimmer S, Iragui V, Katzman R (1989) Abnormal pattern electroretinogram in Alzheimer's disease: evidence for retinal ganglion cell degeneration? *Ann Neurol* 26:221–225. <https://doi.org/10.1002/ana.410260207>
55. Kfoury N, Holmes BB, Jiang H, Holtzman DM, Diamond MI (2012) Trans-cellular propagation of tau aggregation by fibrillar species. *J Biol Chem* 287:19440–19451. <https://doi.org/10.1074/jbc.M112.346072>
56. Kim US, Mahroo OA, Mollon JD, Yu-Wai-Man P (2021) Retinal ganglion cells-diversity of cell types and clinical relevance. *Front Neurol* 12:661938. <https://doi.org/10.3389/fneur.2021.661938>
57. Kirbas S, Turkyilmaz K, Anlar O, Tufekci A, Durmus M (2013) Retinal nerve fiber layer thickness in patients with Alzheimer disease. *J Neuroophthalmol* 33:58–61. <https://doi.org/10.1097/WNO.0b013e318267fd5f>
58. Kivela T (1998) Parvalbumin, a horizontal cell-associated calcium-binding protein in retinoblastoma eyes. *Invest Ophthalmol Vis Sci* 39:1044–1048
59. Kopeikina KJ, Hyman BT, Spiros-Jones TL (2012) Soluble forms of tau are toxic in Alzheimer's disease. *Transl Neurosci* 3:223–233. <https://doi.org/10.2478/s13380-012-0032-y>
60. Koper MJ, Moonen S, Ronisz A, Ospitalieri S, Callaerts-Vegh Z, T'Syen D, Rabe S, Staufienbiel M, De Strooper B, Balusu S et al (2024) Inhibition of an Alzheimer's disease-associated form of necroptosis rescues neuronal death in mouse models. *Sci Transl Med* 16:eadf5128. <https://doi.org/10.1126/scitranslmed.adf5128>
61. Koper MJ, Tome SO, Gawor K, Belet A, Van Schoor E, Schaevebeke J, Vandenberghe R, Vandenbulcke M, Ghebremedhin E, Otto M (2022) LATE-NC aggravates GVD-mediated necroptosis in Alzheimer's disease. *Acta Neuropathol Commun* 10:128. <https://doi.org/10.1186/s40478-022-01432-6>
62. Koper MJ, Van Schoor E, Ospitalieri S, Vandenberghe R, Vandenbulcke M, von Arnim CAF, Tousseyn T, Balusu S, De Strooper B, Thal DR (2020) Necrosome complex detected in granulovacuolar degeneration is associated with neuronal loss in Alzheimer's disease. *Acta Neuropathol* 139:463–484. <https://doi.org/10.1007/s00401-019-02103-y>
63. Koronyo Y, Biggs D, Barron E, Boyer DS, Pearlman JA, Au WJ, Kile SJ, Blanco A, Fuchs DT, Ashfaq A et al (2017) Retinal amyloid pathology and proof-of-concept imaging trial in Alzheimer's disease. *JCI Insight* 2(16):e93621. <https://doi.org/10.1172/jci.insight.93621>
64. Koronyo Y, Rentsendorj A, Mirzaei N, Regis GC, Sheyn J, Shi H, Barron E, Cook-Wiens G, Rodriguez AR, Medeiros R et al (2023) Retinal pathological features and proteome signatures of Alzheimer's disease. *Acta Neuropathol* 145(4):409–438. <https://doi.org/10.1007/s00401-023-02548-2>
65. Koronyo-Hamaoui M, Koronyo Y, Ljubimov AV, Miller CA, Ko MK, Black KL, Schwartz M, Farkas DL (2011) Identification of amyloid plaques in retinas from Alzheimer's patients and noninvasive in vivo optical imaging of retinal plaques in a mouse model. *NeuroImage* 54(Suppl 1):S204–217. <https://doi.org/10.1016/j.neuroimage.2010.06.020>
66. Kwong JM, Caprioli J, Piri N (2010) RNA binding protein with multiple splicing: a new marker for retinal ganglion cells. *Invest Ophthalmol Vis Sci* 51:1052–1058. <https://doi.org/10.1167/iovs.09-4098>
67. Kyalu Ngoie Zola N, Balty C, Pyr Dit Ruys S, Vanparys AAT, Huyghe NDG, Herinckx G, Johannes M, Boyer E, Kienlen-Campard P, Rider MH et al (2023) Specific post-translational modifications of soluble tau protein distinguishes Alzheimer's disease and primary tauopathies. *Nat Commun* 14:3706. <https://doi.org/10.1038/s41467-023-39328-1>
68. La Joie R, Visani AV, Baker SL, Brown JA, Bourakova V, Cha J, Chaudhary K, Edwards L, Iaccarino L, Janabi M et al (2020) Prospective longitudinal atrophy in Alzheimer's disease correlates with the intensity and topography of baseline tau-PET. *Sci Transl Med* 12(524):eaau5732. <https://doi.org/10.1126/scitranslmed.aau5732>
69. La Morgia C, Di Vito L, Carelli V, Carbonelli M (2017) Patterns of retinal ganglion cell damage in neurodegenerative disorders: parvocellular vs Magnocellular Degeneration in Optical Coherence Tomography studies. *Front Neurol* 8:710. <https://doi.org/10.3389/fneur.2017.00710>
70. La Morgia C, Ross-Cisneros FN, Koronyo Y, Hannibal J, Gallassi R, Cantalupo G, Sambati L, Pan BX, Tozer KR, Barboni P et al (2016) Melanopsin retinal ganglion cell loss in Alzheimer disease. *Ann Neurol* 79:90–109. <https://doi.org/10.1002/ana.24548>
71. Lambert MP, Barlow AK, Chromy BA, Edwards C, Freed R, Liosatos M, Morgan TE, Rozovsky I, Trommer B, Viola KL et al (1998) Diffusible, nonfibrillar ligands derived from Abeta1–42 are potent central nervous system neurotoxins. *Proc Natl Acad Sci U S A* 95:6448–6453. <https://doi.org/10.1073/pnas.95.11.6448>
72. Laycock R, Crewther SG, Crewther DP (2007) A role for the 'magnocellular advantage' in visual impairments in neurodevelopmental and psychiatric disorders. *Neurosci Biobehav Rev* 31:363–376. <https://doi.org/10.1016/j.neubiorev.2006.10.003>
73. Lee S, Jiang K, McIlmoyle B, To E, Xu QA, Hirsch-Reinshagen V, Mackenzie IR, Hsiung GR, Eadie BD, Sarunic MV et al (2020) Amyloid Beta immunoreactivity in the retinal ganglion cell layer of the Alzheimer's Eye. *Front Neurosci* 14:758. <https://doi.org/10.3389/fnins.2020.00758>
74. Lemmens S, Van Craenendonck T, Van Eijgen J, De Groef L, Bruffaerts R, de Jesus DA, Charle W, Jayapala M, Sunaric-Megevand G, Standaert A et al (2020) Combination of snapshot hyperspectral retinal imaging and optical coherence tomography to identify Alzheimer's disease patients. *Alzheimers Res Ther* 12:144. <https://doi.org/10.1186/s13195-020-00715-1>
75. Lopez-Cuenca I, Nebreda A, Garcia-Colomo A, Salobrar-Garcia E, de Frutos-Lucas J, Bruna R, Ramirez AI, Ramirez-Torano F, Salazar JJ, Barabash A et al (2023) Early visual alterations in individuals at-risk of Alzheimer's disease: a multidisciplinary approach. *Alzheimers Res Ther* 15:19. <https://doi.org/10.1186/s13195-023-01166-0>
76. Lopez-de-Eguileta A, Lopez-Garcia S, Lage C, Pozueta A, Garcia-Martinez M, Kazimierzczak M, Bravo M, Irure J, Lopez-Hoyos M, Munoz-Cacho P et al (2022) The retinal ganglion cell layer reflects neurodegenerative changes in cognitively unimpaired individuals. *Alzheimers Res Ther* 14:57. <https://doi.org/10.1186/s13195-022-00998-6>
77. Lu Y, Li Z, Zhang X, Ming B, Jia J, Wang R, Ma D (2010) Retinal nerve fiber layer structure abnormalities in early Alzheimer's disease: evidence in optical coherence tomography. *Neurosci Lett* 480:69–72. <https://doi.org/10.1016/j.neulet.2010.06.006>
78. Marziani E, Pomati S, Ramolfo P, Cigada M, Giani A, Mariani C, Staurengi G (2013) Evaluation of retinal nerve fiber layer and ganglion cell layer thickness in Alzheimer's disease using spectral-domain optical coherence tomography. *Invest Ophthalmol Vis Sci* 54:5953–5958. <https://doi.org/10.1167/iovs.13-12046>
79. Miller DT, Kurokawa K (2020) Cellular-Scale imaging of transparent retinal structures and processes using adaptive Optics Optical Coherence Tomography. *Annu Rev Vis Sci* 6:115–148. <https://doi.org/10.1146/annurev-vision-030320-041255>
80. Mirra SS, Heyman A, McKeel D, Sumi SM, Crain BJ, Brownlee LM, Vogel FS, Hughes JP, van Belle G, Berg L (1991) The Consortium to establish a Registry for Alzheimer's Disease (CERAD). Part II. Standardization of the neuropathologic assessment of Alzheimer's disease. *Neurology* 41:479–486. <https://doi.org/10.1212/wnl.41.4.479>
81. Mirzaei N, Shi H, Oviatt M, Doustar J, Rentsendorj A, Fuchs DT, Sheyn J, Black KL, Koronyo Y, Koronyo-Hamaoui M (2020) Alzheimer's retinopathy: seeing Disease in the eyes. *Front Neurosci* 14:921. <https://doi.org/10.3389/fnins.2020.00921>
82. Moloney CM, Lowe VJ, Murray ME (2021) Visualization of neurofibrillary tangle maturity in Alzheimer's disease: a clinicopathologic perspective for biomarker research. *Alzheimers Dement* 17:1554–1574. <https://doi.org/10.1002/alz.12321>
83. Montine TJ, Phelps CH, Beach TG, Bigio EH, Cairns NJ, Dickson DW, Duyckaerts C, Frosch MP, Masliah E, Mirra SS et al (2012) National Institute on Aging-Alzheimer's Association guidelines for the neuropathologic assessment of Alzheimer's disease: a practical approach. *Acta Neuropathol* 123:1–11. <https://doi.org/10.1007/s00401-011-0910-3>
84. More SS, Beach JM, McClelland C, Mokhtazadeh A, Vince R (2019) In vivo Assessment of retinal biomarkers by Hyperspectral Imaging: early detection of Alzheimer's Disease. *ACS Chem Neurosci* 10:4492–4501. <https://doi.org/10.1021/acscchemneuro.9b00331>
85. Morris JC (1993) The clinical dementia rating (CDR): current version and scoring rules. *Neurology* 43:2412–2414. <https://doi.org/10.1212/wnl.43.11.2412-a>
86. Mucke L, Selkoe DJ (2012) Neurotoxicity of amyloid beta-protein: synaptic and network dysfunction. *Cold Spring Harb Perspect Med* 2:a006338. <https://doi.org/10.1101/cshperspect.a006338>
87. Nadal-Nicolás FM, Galindo-Romero C, Lucas-Ruiz F, Marsh-Amstrong N, Li W, Vidal-Sanz M, Agudo-Barrisuso M (2023) Pan-retinal ganglion cell markers in mice, rats, and rhesus macaques. *Zool Res* 44:226–248. <https://doi.org/10.2472/jissn.2095-8137.2022.308>
88. Ngolab J, Donohue M, Belsha A, Salazar J, Cohen P, Jaiswal S, Tan V, Gessert D, Koroury S, Aggarwal NT et al (2021) Feasibility study for detection of retinal amyloid in clinical trials: The Anti-Amyloid Treatment in Asymptomatic Alzheimer's Disease (A4) trial. *Alzheimers Dement (Amst)* 13:e12199. <https://doi.org/10.1002/dad2.12199>
89. Nunez-Diaz C, Andersson E, Schultz N, Pociuciute D, Hansson O, Netherlands Brain B, Nilsson KPR, Wennstrom M (2024) The fluorescent ligand bTVBT2

- reveals increased p-tau uptake by retinal microglia in Alzheimer's disease patients and App(NL-F/NL-F) mice. *Alzheimers Res Ther* 16(1):4. <https://doi.org/10.1186/s13195-023-01375-7>
90. O'Bryant SE, Humphreys JD, Smith GE, Ivnik RJ, Graff-Radford NR, Petersen RC, Lucas JA (2008) Detecting dementia with the mini-mental state examination in highly educated individuals. *Arch Neurol* 65:963–967. <https://doi.org/10.1001/archneur.65.7.963>
 91. Oku H, Kida T, Horie T, Taki K, Mimura M, Kojima S, Ikeda T (2019) Tau is involved in death of retinal ganglion cells of rats from Optic nerve crush. *Invest Ophthalmol Vis Sci* 60:2380–2387. <https://doi.org/10.1167/iov.19-26683>
 92. Pasparakis M, Vandenabeele P (2015) Necroptosis and its role in inflammation. *Nature* 517:311–320. <https://doi.org/10.1038/nature14191>
 93. Peeraer E, Bittelbergs A, Van Kolen K, Stancu IC, Vasconcelos B, Mahieu M, Duytschaever H, Ver Donck L, Torremans A, Sluydts E et al (2015) Intracerebral injection of preformed synthetic tau fibrils initiates widespread tauopathy and neuronal loss in the brains of tau transgenic mice. *Neurobiol Dis* 73:83–95. <https://doi.org/10.1016/j.nbd.2014.08.032>
 94. Pereiro X, Ruzafa N, Urcola JH, Sharma SC, Vecino E (2020) Differential distribution of RBPMS in Pig, Rat, and human retina after Damage. *Int J Mol Sci* 21(23):9330. <https://doi.org/10.3390/ijms21239330>
 95. Piri N, Kwong JM, Song M, Caprioli J (2006) Expression of hermes gene is restricted to the ganglion cells in the retina. *Neurosci Lett* 405:40–45. <https://doi.org/10.1016/j.neulet.2006.06.049>
 96. Puangmalai N, Bhatt N, Montalbano M, Sengupta U, Gaikwad S, Ventura F, McAllen S, Ellsworth A, Garcia S, Kaye R (2020) Internalization mechanisms of brain-derived tau oligomers from patients with Alzheimer's disease, progressive supranuclear palsy and dementia with Lewy bodies. *Cell Death Dis* 11:314. <https://doi.org/10.1038/s41419-020-2503-3>
 97. Purves DAGJ, Fitzpatrick D, Katz LC, LaMantia A-S, McNamara JO, William SM (2001) Neuroscience, 2nd edition. Sunderland (MA): Sinauer Associates, City
 98. Qiu Y, Jin T, Mason E, Campbell MCW (2020) Predicting Thioflavin fluorescence of retinal amyloid deposits Associated with Alzheimer's Disease from their Polarimetric Properties. *Transl Vis Sci Technol* 9:47. <https://doi.org/10.1167/tvst.9.2.47>
 99. Rawat P, Sehar U, Bisht J, Selman A, Culbertson J, Reddy PH (2022) Phosphorylated Tau in Alzheimer's Disease and Other Tauopathies. *Int J Mol Sci* 23(21):12841. <https://doi.org/10.3390/ijms232112841>
 100. Regalado-Reyes M, Furcila D, Hernandez F, Avila J, DeFelipe J, Leon-Espinosa G (2019) Phospho-tau changes in the human CA1 during Alzheimer's Disease Progression. *J Alzheimers Dis* 69:277–288. <https://doi.org/10.3233/JAD-181263>
 101. Risacher SL, WuDunn D, Tallman EF, West JD, Gao S, Farlow MR, Brosch JR, Apostolova LG, Saykin AJ (2020) Visual contrast sensitivity is associated with the presence of cerebral amyloid and tau deposition. *Brain Commun* 2:fcaa019. <https://doi.org/10.1093/braincomms/fcaa019>
 102. Rodriguez AR, de Sevilla Müller LP, Brecha NC (2014) The RNA binding protein RBPMS is a selective marker of ganglion cells in the mammalian retina. *J Comp Neurol* 522:1411–1443. <https://doi.org/10.1002/cne.23521>
 103. Rossetti HC, Munro Cullum C, Hynan LS, Lacritz LH (2010) The CERAD neuropsychologic battery total score and the progression of Alzheimer disease. *Alzheimer Dis Assoc Disord* 24:138–142. <https://doi.org/10.1097/WAD.0b013e3181b76415>
 104. Sadun AA, Borchert M, DeVita E, Hinton DR, Bassi CJ (1987) Assessment of visual impairment in patients with Alzheimer's disease. *Am J Ophthalmol* 104:113–120. [https://doi.org/10.1016/0002-9394\(87\)90001-8](https://doi.org/10.1016/0002-9394(87)90001-8)
 105. Salobar-García E, de Hoz R, Ramirez AI, Lopez-Cuenca I, Rojas P, Vazirani R, Amarante C, Yubero R, Gil P, Pinazo-Duran MD et al (2019) Changes in visual function and retinal structure in the progression of Alzheimer's disease. *PLoS ONE* 14:e0220535. <https://doi.org/10.1371/journal.pone.0220535>
 106. Sanes JR, Masland RH (2015) The types of retinal ganglion cells: current status and implications for neuronal classification. *Annu Rev Neurosci* 38:221–246. <https://doi.org/10.1146/annurev-neuro-071714-034120>
 107. Schön C, Hoffmann NA, Ochs SM, Burgold S, Filser S, Steinbach S, Seeliger MW, Arzberger T, Goedert M, Kretschmar HA et al (2012) Long-term in vivo imaging of fibrillar tau in the retina of P301S transgenic mice. *PLoS ONE* 7:e53547. <https://doi.org/10.1371/journal.pone.0053547>
 108. Schultz N, Byman E, Wennström M (2020) Levels of retinal Amyloid- β correlate with levels of retinal IAPP and hippocampal Amyloid- β in Neuropathologically evaluated individuals. *J Alzheimers Dis* 73:1201–1209. <https://doi.org/10.3233/jad-190868>
 109. Serrano-Pozo A, Frosch MP, Masliah E, Hyman BT (2011) Neuropathological alterations in Alzheimer disease. *Cold Spring Harb Perspect Med* 1:a006189. <https://doi.org/10.1101/cshperspect.a006189>
 110. Shi H, Koronyo Y, Fuchs DT, Sheyn J, Jallow O, Mandalia K, Graham SL, Gupta VK, Mirzaei M, Kramerov AA et al (2023) Retinal arterial A β_{40} deposition is linked with tight junction loss and cerebral amyloid angiopathy in MCI and AD patients. *Alzheimers Dement* 19(11):5185–5197. <https://doi.org/10.1002/alz.13086>
 111. Shi H, Koronyo Y, Rentsendorj A, Regis GC, Sheyn J, Fuchs DT, Kramerov AA, Ljubimov AV, Dumitrascu OM, Rodriguez AR (2020) Identification of early pericyte loss and vascular amyloidosis in Alzheimer's disease retina. *Acta Neuropathol* 139(5):813–836. <https://doi.org/10.1007/s00401-020-02134-w>
 112. Shi H, Mirzaei N, Koronyo Y, Davis MR, Robinson E, Braun GM, Jallow O, Rentsendorj A, Ramanujan VK, Fert-Bober J et al (2024) Identification of retinal oligomeric, citrullinated, and other tau isoforms in early and advanced AD and relations to disease status. *Acta Neuropathol* 148(1):3. <https://doi.org/10.1007/s00401-024-02760-8>
 113. Snyder PJ, Alber J, Alt C, Bain LJ, Bouma BE, Bouwman FH, DeBuc DC, Campbell MCW, Carrillo MC, Chew EY (2021) Retinal imaging in Alzheimer's and neurodegenerative diseases. *Alzheimers Dement* 17: 103–111. <https://doi.org/10.1002/alz.12179>
 114. Sperling RA, Aisen PS, Beckett LA, Bennett DA, Craft S, Fagan AM, Iwatsubo T, Jack CR Jr, Kaye J, Montine TJ et al (2011) Toward defining the preclinical stages of Alzheimer's disease: recommendations from the National Institute on Aging-Alzheimer's Association workgroups on diagnostic guidelines for Alzheimer's disease. *Alzheimers Dement* 7:280–292. <https://doi.org/10.1016/j.jalz.2011.03.003>
 115. Sperling RA, Donohue MC, Raman R, Sun CK, Yaari R, Holdridge K, Siemers E, Johnson KA, Aisen PS, Team AS (2020) Association of factors with elevated amyloid burden in clinically normal older individuals. *JAMA Neurol* 77:735–745. <https://doi.org/10.1001/jama.2020.0387>
 116. Su JH, Zhao M, Anderson AJ, Srinivasan A, Cotman CW (2001) Activated caspase-3 expression in Alzheimer's and aged control brain: correlation with Alzheimer pathology. *Brain Res* 898:350–357. [https://doi.org/10.1016/S0006-8993\(01\)02018-2](https://doi.org/10.1016/S0006-8993(01)02018-2)
 117. Taddei RN, Perbet R, Mate de Gerando A, Wiedmer AE, Sanchez-Mico M, Connors Stewart T, Gaona A, Melloni A, Amaral AC, Duff K et al (2023) Tau oligomer-containing synapse elimination by microglia and astrocytes in Alzheimer disease. *JAMA Neurol* 80:1209–1221. <https://doi.org/10.1001/jama.2023.3530>
 118. Tadokoro K, Yamashita T, Kimura S, Nomura E, Ohta Y, Omote Y, Takemoto M, Hishikawa N, Morihara R, Morizane Y et al (2021) Retinal Amyloid Imaging for Screening Alzheimer's Disease. *J Alzheimers Dis* 83:927–934. <https://doi.org/10.3233/JAD-210327>
 119. Tai HC, Serrano-Pozo A, Hashimoto T, Frosch MP, Spire-Jones TL, Hyman BT (2012) The synaptic accumulation of hyperphosphorylated tau oligomers in Alzheimer disease is associated with dysfunction of the ubiquitin-proteasome system. *Am J Pathol* 181:1426–1435. <https://doi.org/10.1016/j.ajpath.2012.06.033>
 120. Tenhula WN, Xu SZ, Madigan MC, Heller K, Freeman WR, Sadun AA (1992) Morphometric comparisons of optic nerve axon loss in acquired immunodeficiency syndrome. *Am J Ophthalmol* 113:14–20. [https://doi.org/10.1016/S0002-9394\(14\)75746-0](https://doi.org/10.1016/S0002-9394(14)75746-0)
 121. Thal DR, Gawor K, Moonen S (2024) Regulated cell death and its role in Alzheimer's disease and amyotrophic lateral sclerosis. *Acta Neuropathol* 147:69. <https://doi.org/10.1007/s00401-024-02722-0>
 122. Thal DR, Rüb U, Orantes M, Braak H (2002) Phases of a beta-deposition in the human brain and its relevance for the development of AD. *Neurology* 58:1791–1800. <https://doi.org/10.1212/wnl.58.12.1791>
 123. Theofilas P, Ehrenberg AJ, Nguy A, Thackrey JM, Dunlop S, Mejia MB, Alho AT, Parazo Leite RE, Rodriguez RD, Suemoto CK et al (2018) Probing the correlation of neuronal loss, neurofibrillary tangles, and cell death markers across the Alzheimer's disease Braak stages: a quantitative study in humans. *Neurobiol Aging* 61:1–12. <https://doi.org/10.1016/j.neurobiolaging.2017.09.007>
 124. Thomsen ND, Koerber JT, Wells JA (2013) Structural snapshots reveal distinct mechanisms of procaspase-3 and -7 activation. *Proc Natl Acad Sci U S A* 110:8477–8482. <https://doi.org/10.1073/pnas.1306759110>
 125. Trick GL, Barris MC, Bickler-Bluth M (1989) Abnormal pattern electroretinograms in patients with senile dementia of the Alzheimer type. *Ann Neurol* 26:226–231. <https://doi.org/10.1002/ana.410260208>

126. Uchihara T (2007) Silver diagnosis in neuropathology: principles, practice and revised interpretation. *Acta Neuropathol* 113:483–499. <https://doi.org/10.1007/s00401-007-0200-2>
127. van der Gaag BL, Deshayes NAC, Breve JJP, Bol J, Jonker AJ, Hoozemans JJM, Courade JP, van de Berg WDJ (2024) Distinct tau and alpha-synuclein molecular signatures in Alzheimer's disease with and without Lewy bodies and Parkinson's disease with dementia. *Acta Neuropathol* 147:14. <https://doi.org/10.1007/s00401-023-02657-y>
128. VanderWall KB, Lu B, Alfaro JS, Allsop AR, Carr AS, Wang S, Meyer JS (2020) Differential susceptibility of retinal ganglion cell subtypes in acute and chronic models of injury and disease. *Sci Rep* 10:17359. <https://doi.org/10.1038/s41598-020-71460-6>
129. Walkiewicz G, Ronisz A, Van Ginderdeuren R, Lemmens S, Bouwman FH, Hoozemans JJM, Morrema THJ, Rozemuller AJ, Hart de Ruyter FJ, De Groef L et al (2024) Primary retinal tauopathy: a tauopathy with a distinct molecular pattern. *Alzheimers Dement* 20(1):330–340. <https://doi.org/10.1002/alz.13424>
130. Wiersma VI, Hoozemans JJM, Scheper W (2020) Untangling the origin and function of granulovacuolar degeneration bodies in neurodegenerative proteinopathies. *Acta Neuropathol Commun* 8(1):153. <https://doi.org/10.1186/s40478-020-00996-5>
131. Xu QA, Boerkoel P, Hirsch-Reinshagen V, Mackenzie IR, Hsiung GR, Charm G, To EF, Liu AQ, Schwab K, Jiang K et al (2022) Muller cell degeneration and microglial dysfunction in the Alzheimer's retina. *Acta Neuropathol Commun* 10:145. <https://doi.org/10.1186/s40478-022-01448-y>
132. Yarns BC, Holiday KA, Carlson DM, Cosgrove CK, Melrose RJ (2022) Pathophysiology of Alzheimer's Disease. *Psychiatr Clin North Am* 45:663–676. <https://doi.org/10.1016/j.psc.2022.07.003>
133. Zhang R, Song Y, Su X (2023) Necroptosis and Alzheimer's Disease: pathogenic mechanisms and Therapeutic opportunities. *J Alzheimers Dis* 94:S367–S386. <https://doi.org/10.3233/JAD-220809>
134. Zhang Y, Chen H, Li R, Sterling K, Song W (2023) Amyloid beta-based therapy for Alzheimer's disease: challenges, successes and future. *Signal Transduct Target Ther* 8:248. <https://doi.org/10.1038/s41392-023-01484-7>
135. Zhao B, Li Y, Fan Z, Wu Z, Shu J, Yang X, Yang Y, Wang X, Li B, Wang X et al (2024) Eye-brain connections revealed by multimodal retinal and brain imaging genetics. *Nat Commun* 15:6064. <https://doi.org/10.1038/s41467-024-50309-w>

Publisher's note

Springer Nature remains neutral with regard to jurisdictional claims in published maps and institutional affiliations.